

# Dual Formulation Finite-Volume Methods on Overlapping Meshes for Hyperbolic Conservation Laws

Rémi Abgrall\*, Alina Chertock†, Alexander Kurganov‡, and Lorenzo Micalizzi§

## Abstract

In this work, we introduce new second-order schemes for one- and two-dimensional hyperbolic systems of conservation laws. Following an approach recently proposed in [R. ABGRALL, Commun. Appl. Math. Comput., 5 (2023), pp. 370–402], we consider two different formulations of the studied system (the original conservative formulation and a primitive one containing nonconservative products), and discretize them on overlapping staggered meshes using two different numerical schemes. The novelty of our approach is twofold. First, we introduce an original paradigm making use of overlapping finite-volume (FV) meshes over which cell averages of conservative and primitive variables are evolved using semi-discrete FV methods: The nonconservative system is discretized by a path-conservative central-upwind scheme, and its solution is used to evaluate very simple numerical fluxes for the discretization of the original conservative system. Second, to ensure the nonlinear stability of the resulting method, we design a post-processing, which also guarantees a conservative coupling between the two sets of variables. We test the proposed semi-discrete dual formulation finite-volume methods on several benchmarks for the Euler equations of gas dynamics.

**Key words:** Dual formulation finite-volume methods; overlapping staggered meshes; path-conservative central-upwind schemes; conservative post-processing.

**AMS subject classification:** 76M12, 65M08, 76N99, 35L65, 35L67.

## 1 Introduction

This paper focuses on the development of numerical methods for hyperbolic systems of conservation laws, which in the two-dimensional (2-D) case read as

$$\mathbf{U}_t + \mathbf{F}(\mathbf{U})_x + \mathbf{G}(\mathbf{U})_y = 0. \quad (1.1)$$

Here,  $x$  and  $y$  are the spatial variables,  $t$  is time,  $\mathbf{U} \in \mathbb{R}^M$  is the vector of conserved variables,  $\mathbf{F}, \mathbf{G} \in \mathbb{R}^M$  are the fluxes, whose Jacobians,  $\frac{\partial \mathbf{F}}{\partial \mathbf{U}}, \frac{\partial \mathbf{G}}{\partial \mathbf{U}} \in \mathbb{R}^{M \times M}$ , are assumed to be real-diagonalizable, and  $M \in \mathbb{N}$  with  $M \geq 1$  being the number of equations in the system.

---

\*Institute for Mathematics & Computational Science, University of Zurich, 8057 Zurich, Switzerland; remi.abgrall@math.uzh.ch

†Department of Mathematics, North Carolina State University, Raleigh, NC 27695, USA; chertock@math.ncsu.edu

‡Department of Mathematics and Shenzhen International Center for Mathematics, Southern University of Science and Technology, Shenzhen, 518055, China; alexander@sustech.edu.cn

§Department of Mathematics, North Carolina State University, Raleigh, NC 27695, USA; lmicali@ncsu.edu

It is well-known that solutions of nonlinear hyperbolic conservation laws may become nonsmooth even when the initial and boundary data are infinitely smooth. Therefore, the solution of (1.1) has to be defined in a weak (integral) sense, and hence conservative finite-volume (FV) methods seem to be one of the natural choices to be considered. In these methods, the computational domain is covered by FV cells and the numerical solution is realized in terms of cell averages of conserved variables, which are evolved in time using an integral form of (1.1). For a variety of existing FV methods, we refer the reader to [19, 22, 29, 48] and references therein.

In this work, we are interested in schemes which make use of different formulations of the same governing equations, namely, conservative and nonconservative (primitive) formulations. Examples of such schemes are the active flux (AF) schemes introduced in [1], in which cell averages of conserved variables and point values of primitive ones at cell interfaces are considered. Such additional degrees of freedom with respect to a standard FV scheme can be used not only to enhance the accuracy of the resulting scheme, but also to hybridize conservative and nonconservative numerical methods successfully. We refer the reader to [2, 4, 9, 40], where a clever use of primitive formulations of the governing equations was made. On the other hand, we stress that nonconservative methods per se cannot be used for accurately solving hyperbolic systems of conservation laws since nonconservative numerical schemes typically converge to non-entropy (non-physical) weak solutions, as demonstrated in [3, 23].

A similar idea of obtaining additional degrees of freedom by evolving several pieces of information was used in the methods on overlapping cells. These methods include both FV [31, 33, 34, 50] and discontinuous Galerkin [32, 50, 51] ones. In the FV methods on overlapping cells, hierarchical reconstruction limiters are used to achieve high-order non-oscillatory approximations of the computed solution, whose cell averages on overlapping cells are evolved in time.

In this paper, we develop a novel second-order semi-discrete dual formulation finite-volume (DF-FV) method. To this end, we first consider the following nonconservative system, which is equivalent to (1.1) for smooth solutions:

$$\mathbf{V}_t + \tilde{\mathbf{F}}(\mathbf{V})_x + \tilde{\mathbf{G}}(\mathbf{V})_y = B(\mathbf{V})\mathbf{V}_x + C(\mathbf{V})\mathbf{V}_y, \quad (1.2)$$

where  $\mathbf{V} \in \mathbb{R}^M$  is the vector of primitive variables,  $\tilde{\mathbf{F}}, \tilde{\mathbf{G}} : \mathbb{R}^M \rightarrow \mathbb{R}^M$ , and  $B, C \in \mathbb{R}^{M \times M}$ . To cite an example, one may consider the Euler equations of gas dynamics, which read as (1.1) with

$$\mathbf{U} = (\rho, \rho u, \rho v, E)^\top, \quad \mathbf{F}(\mathbf{U}) = (\rho u, \rho u^2 + p, \rho uv, u(E+p))^\top, \quad \mathbf{G}(\mathbf{U}) = (\rho v, \rho uv, \rho v^2 + p, v(E+p))^\top, \quad (1.3)$$

where  $\rho$  is the density,  $u$  and  $v$  are the  $x$ - and  $y$ -velocities,  $E$  is the total energy, and  $p$  is the pressure. We use the classical closure, obtained with the help of the equation of state of ideal fluids,

$$E = \frac{p}{\gamma - 1} + \frac{1}{2}\rho(u^2 + v^2), \quad (1.4)$$

in which  $\gamma$  is the specific heat ratio. The system (1.1), (1.3)–(1.4) can be rewritten in the nonconservative form in many different ways, for instance, using the primitive variables  $\rho$ ,  $u$ ,  $v$ , and  $p$ , for which the corresponding nonconservative system reads as (1.2) with

$$\mathbf{V} = (\rho, u, v, p)^\top, \quad \tilde{\mathbf{F}}(\mathbf{V}) = \left( \rho u, \frac{u^2}{2}, 0, pu \right)^\top, \quad \tilde{\mathbf{G}}(\mathbf{V}) = \left( \rho v, 0, \frac{v^2}{2}, pv \right)^\top,$$

$$B(\mathbf{V}) = \begin{pmatrix} 0 & 0 & 0 & 0 \\ 0 & 0 & 0 & -\frac{1}{\rho} \\ 0 & 0 & -u & 0 \\ 0 & -(\gamma - 1)p & 0 & 0 \end{pmatrix}, \quad C(\mathbf{V}) = \begin{pmatrix} 0 & 0 & 0 & 0 \\ 0 & -v & 0 & 0 \\ 0 & 0 & 0 & -\frac{1}{\rho} \\ 0 & 0 & -(\gamma - 1)p & 0 \end{pmatrix}.$$

We discretize the systems (1.1) and (1.2) on overlapping meshes using a semi-discrete approach, and then solve the resulting systems of ordinary differential equations (ODEs) simultaneously. The numerical fluxes for the conservative system (1.1) are taken simply as  $\mathbf{F}(\mathbf{U}(\mathbf{V}))$  and  $\mathbf{G}(\mathbf{U}(\mathbf{V}))$ , while the discretization of the nonconservative system (1.2) is more involved as its solutions cannot be understood in the sense of distributions. In [14], a concept of Borel measure solutions of nonconservative systems was introduced (see also [27, 28]) and later utilized to develop path-conservative numerical methods; see, e.g., [6–8, 38, 39] and references therein. Here, we discretize (1.2) using a modified version of the Riemann-problem-solver-free path-conservative central-upwind (PCCU) scheme from [8]. The modification is intended to reduce the amount of numerical dissipation present in the original PCCU scheme and is carried out by replacing the central-upwind (CU) numerical flux from [25], which was used in [8], with a less dissipative CU numerical flux from [24].

Since the conservative numerical fluxes do not employ any limiting procedures, one can expect the computed  $\mathbf{U}$  to be oscillatory. At the same time, variables  $\mathbf{V}$ , computed in a non-oscillatory manner by the PCCU scheme, may converge to a non-physical weak solution. We therefore introduce a conservative post-processing, which couples the evolution of the two sets of variables. The resulting numerical solution is (essentially) oscillation-free and the scheme converges to the physically relevant solution of (1.1).

We test the proposed DF-FV methods on several benchmarks for one- and two-dimensional Euler equations of gas dynamics. In these examples, we also demonstrate that the 1-D DF-FV method outperforms the second-order central scheme on overlapping cells from [31].

The rest of the paper is organized as follows. In §2, we introduce the new one-dimensional (1-D) DF-FV method, and then extend it to the 2-D case in §3. In §4, we report the results of several numerical experiments for both 1-D and 2-D Euler equations of gas dynamics. Finally, in §5, we provide concluding remarks and discuss future perspectives.

## 2 One-Dimensional Semi-Discrete DF-FV Method

In this section, we introduce the new semi-discrete DF-FV method for the 1-D version of (1.1):

$$\mathbf{U}_t + \mathbf{F}(\mathbf{U})_x = 0, \quad (2.1)$$

whose nonconservative formulation reads as

$$\mathbf{V}_t + \tilde{\mathbf{F}}(\mathbf{V})_x = \mathbf{B}(\mathbf{V})\mathbf{V}_x. \quad (2.2)$$

We consider overlapping FV meshes consisting of uniform cells  $I_j = [x_{j-\frac{1}{2}}, x_{j+\frac{1}{2}}]$ ,  $j = 1, \dots, N$  and  $I_{j+\frac{1}{2}} = [x_j, x_{j+1}]$ ,  $j = 0, \dots, N$  with  $x_{j+1} = x_{j+\frac{1}{2}} + \Delta x/2 = x_j + \Delta x$  for all  $j$ . As in all FV methods, the computed quantities are cell averages of  $\mathbf{U}$  and  $\mathbf{V}$ , which are obtained on the above two grids, namely,

$$\bar{\mathbf{U}}_j := \frac{1}{\Delta x} \int_{I_j} \mathbf{U}(x, t) dx \quad \text{and} \quad \bar{\mathbf{V}}_{j+\frac{1}{2}} := \frac{1}{\Delta x} \int_{I_{j+\frac{1}{2}}} \mathbf{V}(x, t) dx.$$

Note that both  $\bar{\mathbf{U}}_j$  and  $\bar{\mathbf{V}}_{j+\frac{1}{2}}$ , like many other indexed quantities below, depend on time, but we omit this dependence for the sake of notation brevity.

The semi-discretization of the conservative system (2.1) is obtained by integrating (2.1) in space over the cells  $I_j$ , which results in

$$\frac{d}{dt} \bar{\mathbf{U}}_j = -\frac{1}{\Delta x} [\mathcal{F}_{j+\frac{1}{2}} - \mathcal{F}_{j-\frac{1}{2}}], \quad (2.3)$$

in which we take the following simple numerical fluxes:

$$\mathcal{F}_{j+\frac{1}{2}} = \mathbf{F}(\mathbf{U}_{j+\frac{1}{2}}), \quad \mathbf{U}_{j+\frac{1}{2}} := \mathbf{U}(\bar{\mathbf{V}}_{j+\frac{1}{2}}), \quad (2.4)$$

where  $\mathbf{U}(\mathbf{V})$  denotes the transformation from primitive to conserved variables. Note that for second-order methods, cell averages and point values formally differ by  $\mathcal{O}((\Delta x)^2)$ , which makes the transformation used in (2.4) straightforward, while higher order extensions would require a suitable higher order reconstruction of point values.

The semi-discretization of the nonconservative system (2.2) is obtained through the modified PCCU scheme and reads

$$\frac{d}{dt} \bar{\mathbf{V}}_{j+\frac{1}{2}} = -\frac{1}{\Delta x} [\tilde{\mathcal{F}}_{j+1} - \tilde{\mathcal{F}}_j - \mathbf{B}_{j+\frac{1}{2}} - \frac{a_j^+}{a_j^+ - a_j^-} \mathbf{B}_{\Psi,j} + \frac{a_{j+1}^-}{a_{j+1}^+ - a_{j+1}^-} \mathbf{B}_{\Psi,j+1}], \quad (2.5)$$

where  $\tilde{\mathcal{F}}_j$  are the CU numerical fluxes from [24] given by

$$\tilde{\mathcal{F}}_j = \frac{a_j^+ \tilde{\mathbf{F}}(\mathbf{V}_j^-) - a_j^- \tilde{\mathbf{F}}(\mathbf{V}_j^+)}{a_j^+ - a_j^-} + \frac{a_j^+ a_j^-}{a_j^+ - a_j^-} (\mathbf{V}_j^+ - \mathbf{V}_j^- - \delta \mathbf{V}_j). \quad (2.6)$$

Here,  $\mathbf{V}_j^\pm$  are one-sided point values of  $\mathbf{V}$  obtained using a piecewise linear reconstruction applied to the local characteristic variables  $\Gamma$  oferef 1.2. To this end, we follow [36, 37] and introduce

$$\Gamma_{j-\frac{1}{2}} = Q_{j+\frac{1}{2}}^{-1} \bar{\mathbf{V}}_{j-\frac{1}{2}}, \quad \Gamma_{j+\frac{1}{2}} = Q_{j+\frac{1}{2}}^{-1} \bar{\mathbf{V}}_{j+\frac{1}{2}}, \quad \Gamma_{j+\frac{3}{2}} = Q_{j+\frac{1}{2}}^{-1} \bar{\mathbf{V}}_{j+\frac{3}{2}},$$

where  $Q_{j+\frac{1}{2}}$  is a matrix such that  $Q_{j+\frac{1}{2}}^{-1} \mathcal{A}_{j+\frac{1}{2}} Q_{j+\frac{1}{2}}$  is a diagonal matrix and  $\mathcal{A}_{j+\frac{1}{2}} = \mathcal{A}(\bar{\mathbf{V}}_{j+\frac{1}{2}}) := \frac{\partial \tilde{\mathbf{F}}}{\partial \mathbf{V}}(\bar{\mathbf{V}}_{j+\frac{1}{2}}) - \mathbf{B}(\bar{\mathbf{V}}_{j+\frac{1}{2}})$ . Equipped with  $\Gamma_{j-\frac{1}{2}}$ ,  $\Gamma_{j+\frac{1}{2}}$ , and  $\Gamma_{j+\frac{3}{2}}$ , we apply a generalized minmod limiter (see, e.g., [30, 46]) to evaluate

$$(\Gamma_x)_{j+\frac{1}{2}} = \text{minmod} \left( \theta \frac{\Gamma_{j+\frac{1}{2}} - \Gamma_{j-\frac{1}{2}}}{\Delta x}, \frac{\Gamma_{j+\frac{3}{2}} - \Gamma_{j-\frac{1}{2}}}{2\Delta x}, \theta \frac{\Gamma_{j+\frac{3}{2}} - \Gamma_{j+\frac{1}{2}}}{\Delta x} \right), \quad \theta \in [1, 2],$$

where the minmod function, defined as

$$\text{minmod}(c_1, c_2, \dots) = \begin{cases} \min_i c_i & \text{if } c_i > 0 \ \forall i, \\ \max_i c_i & \text{if } c_i < 0 \ \forall i, \\ 0 & \text{otherwise,} \end{cases}$$

is applied in a component-wise manner. We then obtain

$$\Gamma_j^+ = \Gamma_{j+\frac{1}{2}} - \frac{\Delta x}{2} (\Gamma_x)_{j+\frac{1}{2}}, \quad \Gamma_{j+1}^- = \Gamma_{j+\frac{1}{2}} + \frac{\Delta x}{2} (\Gamma_x)_{j+\frac{1}{2}},$$

and hence the corresponding point values of  $\mathbf{V}$  are

$$\mathbf{V}_j^+ = Q_{j+\frac{1}{2}} \Gamma_j^+, \quad \mathbf{V}_{j+1}^- = Q_{j+\frac{1}{2}} \Gamma_{j+1}^-.$$

In (2.5) and (2.6),  $a_j^\pm$  are the one-sided local speeds of propagation, which can be estimated by

$$a_j^- = \min \{ \lambda_1(\mathbf{V}_j^-), \lambda_1(\mathbf{V}_j^+), 0 \}, \quad a_j^+ = \max \{ \lambda_M(\mathbf{V}_j^-), \lambda_M(\mathbf{V}_j^+), 0 \}.$$

where  $\lambda_1(\mathbf{V}) \leq \dots \leq \lambda_M(\mathbf{V})$  are the eigenvalues of  $\mathcal{A}(\mathbf{V})$ . The term  $\delta\mathbf{V}_j$  in (2.6) represents a “built-in” anti-diffusion and is given by (see [24]),

$$\delta\mathbf{V}_j = \text{minmod}(\mathbf{V}_j^* - \mathbf{V}_j^-, \mathbf{V}_j^+ - \mathbf{V}_j^*), \quad \mathbf{V}_j^* := \frac{a_j^+ \mathbf{V}_j^+ - a_j^- \mathbf{V}_j^- - \tilde{\mathbf{F}}(\mathbf{V}_j^+) + \tilde{\mathbf{F}}(\mathbf{V}_j^-)}{a_j^+ - a_j^-}.$$

Finally, the terms  $\mathbf{B}_{j+\frac{1}{2}}$  and  $\mathbf{B}_{\Psi,j}$  in (2.5) are given by

$$\mathbf{B}_{j+\frac{1}{2}} = B(\bar{\mathbf{V}}_{j+\frac{1}{2}})(\mathbf{V}_{j+1}^- - \mathbf{V}_j^+), \quad \mathbf{B}_{\Psi,j} = \frac{1}{2} [B(\mathbf{V}_j^-) + B(\mathbf{V}_j^+)] (\mathbf{V}_j^+ - \mathbf{V}_j^-),$$

where the former term is obtained by applying a second-order quadrature to  $\int_{I_j} B(\mathbf{V}) \mathbf{V} \, dx$  and the latter one is derived using a linear path connecting  $\mathbf{V}_j^-$  with  $\mathbf{V}_j^+$ ; see [8] for details.

**Remark 2.1** It should be observed that the numerical flux (2.6) is different from the one used in the original version of the PCCU scheme introduced in [8]. The difference is attributed to the presence of the anti-diffusion term  $\delta\mathbf{V}_j$  that helps to reduce the numerical dissipation present in the PCCU scheme and thus to enhance the resolution of contact waves as it was demonstrated in [24], where the conservative formulation of the compressible Euler equations was considered.

**Remark 2.2** We would like to stress that the proposed DF-FV method is not tied to the PCCU scheme and, in principle, one can numerically solve the nonconservative system (2.2) using an alternative second-order stable numerical method instead. However, the PCCU scheme seems to be a reasonable choice, thanks to its distinctive feature: once the path has been selected, the resulting method is not sensitive to a particular choice on the nonconservative formulation; see [8].

The ODE systems (2.3) and (2.5) should be numerically solved by a stable and sufficiently accurate ODE solver. However, the solution obtained upon completion of a time step evolution will have two significant drawbacks. First, the solution realized by  $\{\bar{\mathbf{U}}_j(t + \Delta t)\}$  will likely be oscillatory since no limiting procedures are employed in the computation of numerical fluxes in (2.4). Second, the solution realized by  $\{\bar{\mathbf{V}}_{j+\frac{1}{2}}(t + \Delta t)\}$  will not necessarily be conservative, that is,  $\sum_j \mathbf{U}(\bar{\mathbf{V}}_{j+\frac{1}{2}}(t + \Delta t))$  may not be equal to  $\sum_j \mathbf{U}(\bar{\mathbf{V}}_{j+\frac{1}{2}}(t))$ . Therefore, to ensure that the resulting numerical solution is (essentially) oscillation-free and converges to the physically relevant solution of (2.1), we propose the conservative post-processing procedure presented in the next subsection.

## 2.1 Post-Processing

Let us assume that the solution was evolved from time  $t$  to  $t + \Delta t$  with the help of an ODE solver, and denote the obtained solutions by  $\{\bar{\mathbf{U}}_j^*\}$  and  $\{\bar{\mathbf{V}}_{j+\frac{1}{2}}^*\}$ . Our goal is to modify these values through a suitable post-processing procedure to obtain non-oscillatory sets of  $\{\bar{\mathbf{U}}_j(t + \Delta t)\}$  and  $\{\bar{\mathbf{V}}_{j+\frac{1}{2}}(t + \Delta t)\}$ .

The proposed post-processing can be presented algorithmically through the following four steps.

**Step 1.** Compute the conserved variables at  $x = x_{j+\frac{1}{2}}$  using the transformation from the primitive ones:

$$\mathbf{U}_{j+\frac{1}{2}}^* := \mathbf{U}(\bar{\mathbf{V}}_{j+\frac{1}{2}}^*).$$

**Step 2.** Perform the piecewise linear reconstruction for  $\mathbf{U}$  using the slopes computed by the minmod limiter

$$(\mathbf{U}_x)_j^* = 2 \text{minmod} \left( \frac{\bar{\mathbf{U}}_j^* - \mathbf{U}_{j-\frac{1}{2}}^*}{\Delta x}, \frac{\mathbf{U}_{j+\frac{1}{2}}^* - \bar{\mathbf{U}}_j^*}{\Delta x} \right),$$

which results in

$$\mathbf{U}_{j+\frac{1}{2}}^{*,-} := \bar{\mathbf{U}}_j^* + \frac{\Delta x}{2} (\mathbf{U}_x)_j^*, \quad \mathbf{U}_{j+\frac{1}{2}}^{*,+} := \bar{\mathbf{U}}_{j+1}^* - \frac{\Delta x}{2} (\mathbf{U}_x)_{j+1}^*. \quad (2.7)$$

**Step 3.** Set

$$\mathbf{U}_{j+\frac{1}{2}}^{**} := \frac{1}{2} (\mathbf{U}_{j+\frac{1}{2}}^{*,-} + \mathbf{U}_{j+\frac{1}{2}}^{*,+}), \quad (2.8)$$

and recompute the primitive variables at  $x = x_{j+\frac{1}{2}}$  using the transformation from the conservative ones:

$$\bar{\mathbf{V}}_{j+\frac{1}{2}}(t + \Delta t) = \mathbf{V}(\mathbf{U}_{j+\frac{1}{2}}^{**}).$$

**Step 4.** Correct the conserved variables by setting

$$\bar{\mathbf{U}}_j(t + \Delta t) = \frac{1}{2} (\mathbf{U}_{j-\frac{1}{2}}^{**} + \mathbf{U}_{j+\frac{1}{2}}^{**}). \quad (2.9)$$

It is essential to emphasize that the post-processing is conservative, as demonstrated in the following proposition.

**Proposition 2.1** *The post-processed cell averages of the conserved variables satisfy*

$$\sum_j \bar{\mathbf{U}}_j(t + \Delta t) = \sum_j \bar{\mathbf{U}}_j^*.$$

*Proof.* The proof consists of simple direct computations (assuming no contributions from the boundary terms):

$$\begin{aligned} \sum_j \bar{\mathbf{U}}_j(t + \Delta t) &\stackrel{(2.9)}{=} \frac{1}{2} \sum_j \mathbf{U}_{j-\frac{1}{2}}^{**} + \frac{1}{2} \sum_j \mathbf{U}_{j+\frac{1}{2}}^{**} = \sum_j \mathbf{U}_{j+\frac{1}{2}}^{**} \stackrel{(2.8)}{=} \frac{1}{2} \sum_j \mathbf{U}_{j+\frac{1}{2}}^{*,-} + \frac{1}{2} \sum_j \mathbf{U}_{j+\frac{1}{2}}^{*,+} \\ &\stackrel{(2.7)}{=} \frac{1}{2} \sum_j \left[ \bar{\mathbf{U}}_j^* + \frac{\Delta x}{2} (\mathbf{U}_x)_j^* \right] + \frac{1}{2} \sum_j \left[ \bar{\mathbf{U}}_{j+1}^* - \frac{\Delta x}{2} (\mathbf{U}_x)_{j+1}^* \right] = \sum_j \bar{\mathbf{U}}_j^*. \end{aligned}$$

□

## 2.2 Linear Stability Analysis

It is instructive to study a linear  $L^\infty$  stability of the developed DF-FV method. To this end, we apply the scheme to the linear advection equation

$$U_t + aU_x = 0, \quad (2.10)$$

where  $a$  is a positive constant. In this case, the conservative and primitive formulations coincide, and nonconservative products are not present.

For the sake of simplicity, we apply the first-order forward Euler time discretization, for which the fully discrete DF-FV scheme can be written as follows. Starting from the discrete solution  $\bar{\mathbf{U}}_j(t), \bar{\mathbf{U}}_{j+\frac{1}{2}}(t)$ ,

we first reconstruct the point values  $U_j^\pm(t)$  from  $\bar{U}_{j+\frac{1}{2}}(t)$  using a generalized minmod limiter. We then evolve both  $\bar{U}_j$  and  $\bar{U}_{j+\frac{1}{2}}$  in time to obtain

$$\bar{U}_{j+\frac{1}{2}}^* = \bar{U}_{j+\frac{1}{2}}(t) - \frac{a\Delta t}{\Delta x} [U_{j+1}^-(t) - U_j^-(t)], \quad (2.11)$$

$$\bar{U}_j^* = \bar{U}_j(t) - \frac{a\Delta t}{\Delta x} [U_{j+\frac{1}{2}}(t) - U_{j-\frac{1}{2}}(t)], \quad (2.12)$$

where (2.11) is, in fact, a second-order (in space) upwind scheme, which the PCCU scheme reduces to when applied to the linear advection (2.10) with  $a > 0$ . Next, we apply the post-processing from §2.1. Namely, we compute the reconstructed interface values  $U_{j+\frac{1}{2}}^{*,\pm}$  using (2.7) and evaluate

$$\bar{U}_{j+\frac{1}{2}}(t + \Delta t) = \frac{1}{2} [U_{j+\frac{1}{2}}^{*,-} + U_{j+\frac{1}{2}}^{*,+}] \quad (2.13)$$

and

$$\bar{U}_j(t + \Delta t) = \frac{1}{2} [\bar{U}_{j-\frac{1}{2}}(t + \Delta t) + \bar{U}_{j+\frac{1}{2}}(t + \Delta t)]. \quad (2.14)$$

We now assume the bounds  $\|\bar{U}_{j+\frac{1}{2}}(t)\|_\infty \leq K$  and  $\|\bar{U}_j(t)\|_\infty \leq K$  and prove that the updated values  $\|\bar{U}_{j+\frac{1}{2}}(t + \Delta t)\|_\infty$  and  $\|\bar{U}_j(t + \Delta t)\|_\infty$  remain bounded by  $K$ . First, we observe that (2.11) can be rewritten as

$$\bar{U}_{j+\frac{1}{2}}^* = \frac{U_j^+(t) + U_{j+1}^-(t)}{2} - \frac{a\Delta t}{\Delta x} [U_{j+1}^-(t) - U_j^-(t)] = \left(\frac{1}{2} - \frac{a\Delta t}{\Delta x}\right) U_{j+1}^-(t) + \frac{1}{2} U_j^+(t) + \frac{a\Delta t}{\Delta x} U_j^-(t).$$

Imposing the CFL condition

$$\frac{a\Delta t}{\Delta x} \leq \frac{1}{2} \quad (2.15)$$

and using the non-oscillatory nature of the generalized minmod reconstruction that ensures  $|U_j^\pm| \leq K$ , we obtain

$$|\bar{U}_{j+\frac{1}{2}}^*| \leq \left(\frac{1}{2} - \frac{a\Delta t}{\Delta x}\right) |U_{j+1}^-(t)| + \frac{1}{2} |U_j^+(t)| + \frac{a\Delta t}{\Delta x} |U_j^-(t)| \leq \left(\frac{1}{2} - \frac{a\Delta t}{\Delta x} + \frac{1}{2} + \frac{a\Delta t}{\Delta x}\right) K = K. \quad (2.16)$$

Next, (2.12) together with (2.14), written at the previous time level  $t$  rather than at  $t + \Delta t$ , yields

$$\bar{U}_j^* = \frac{\bar{U}_{j+\frac{1}{2}}(t) + \bar{U}_{j-\frac{1}{2}}(t)}{2} - \frac{a\Delta t}{\Delta x} [\bar{U}_{j+\frac{1}{2}}(t) - \bar{U}_{j-\frac{1}{2}}(t)] = \left(\frac{1}{2} - \frac{a\Delta t}{\Delta x}\right) \bar{U}_{j+\frac{1}{2}}(t) + \left(\frac{1}{2} + \frac{a\Delta t}{\Delta x}\right) \bar{U}_{j-\frac{1}{2}}(t),$$

which, under the same CFL restriction (2.15), leads to

$$|\bar{U}_j^*| \leq \left(\frac{1}{2} - \frac{a\Delta t}{\Delta x}\right) |\bar{U}_{j+\frac{1}{2}}(t)| + \left(\frac{1}{2} + \frac{a\Delta t}{\Delta x}\right) |\bar{U}_{j-\frac{1}{2}}(t)| \leq \left(\frac{1}{2} - \frac{a\Delta t}{\Delta x} + \frac{1}{2} + \frac{a\Delta t}{\Delta x}\right) K = K. \quad (2.17)$$

Finally, combining equations (2.13)–(2.14) with the bounds (2.16)–(2.17), and noting once again that the generalized minmod reconstruction is non-oscillatory and satisfies  $|U_{j+\frac{1}{2}}^{*,\pm}| \leq K$ , we conclude that both  $\bar{U}_{j+\frac{1}{2}}(t + \Delta t)$  and  $\bar{U}_j(t + \Delta t)$  remain bounded by  $K$ . This establishes the  $L^\infty$  stability of the DF–FV method for linear problems (2.10) under the CFL condition (2.15).

### 3 Two-Dimensional Semi-Discrete DF-FV Method

We now extend the proposed semi-discrete DF-FV method to the 2-D case, in which the conservative and nonconservative (primitive) formulations of the governing equations are given by (1.1) and (1.2), respectively.

We consider overlapping Cartesian meshes (see the sketch in Figure 3.1) consisting of uniform cells  $I_{j,k} := [x_{j-\frac{1}{2}}, x_{j+\frac{1}{2}}] \times [y_{k-\frac{1}{2}}, y_{k+\frac{1}{2}}]$ ,  $j = 1, \dots, N_x$ ,  $k = 1, \dots, N_y$ ,  $I_{j+\frac{1}{2},k}^x = [x_j, x_{j+1}] \times [y_{k-\frac{1}{2}}, y_{k+\frac{1}{2}}]$ ,  $j = 0, \dots, N_x$ ,  $k = 1, \dots, N_y$ , and  $I_{j,k+\frac{1}{2}}^y = [x_{j-\frac{1}{2}}, x_{j+\frac{1}{2}}] \times [y_k, y_{k+1}]$ ,  $j = 1, \dots, N_x$ ,  $k = 0, \dots, N_y$  with  $x_{j+1} = x_{j+\frac{1}{2}} + \Delta x/2 = x_j + \Delta x$  for all  $j$  and  $y_{k+1} = y_{k+\frac{1}{2}} + \Delta y/2 = y_k + \Delta y$  for all  $k$ . The computed quantities are the following cell averages obtained on the above three grids:

$$\bar{\mathbf{U}}_{j,k} := \frac{1}{\Delta x \Delta y} \int_{I_{j,k}} \mathbf{U}(x, t) dx dy, \quad \bar{\mathbf{V}}_{j+\frac{1}{2},k}^x := \frac{1}{\Delta x \Delta y} \int_{I_{j+\frac{1}{2},k}^x} \mathbf{V}(x, t) dx dy, \quad \bar{\mathbf{V}}_{j,k+\frac{1}{2}}^y := \frac{1}{\Delta x \Delta y} \int_{I_{j,k+\frac{1}{2}}^y} \mathbf{V}(x, t) dx dy.$$

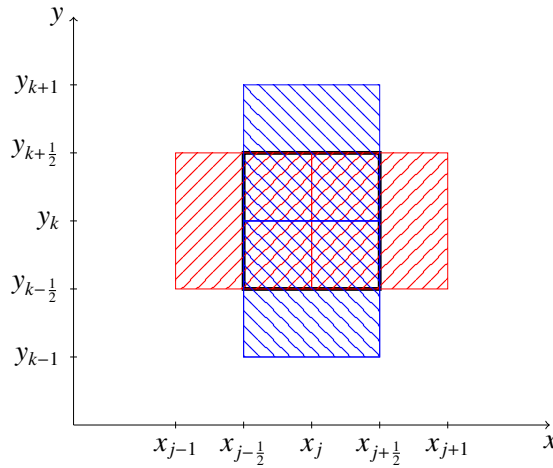


Figure 3.1: Sketch of the overlapping cells:  $I_{j,k}$  (black-bordered);  $I_{j-\frac{1}{2},k}^x$  and  $I_{j+\frac{1}{2},k}^x$  (red-filled);  $I_{j,k-\frac{1}{2}}^y$  and  $I_{j,k+\frac{1}{2}}^y$  (blue-filled).

As in the 1-D case, the semi-discretization of the conservative system (1.1) is obtained by integrating (1.1) in space over the cells  $I_{j,k}$ , which leads to

$$\frac{d}{dt} \bar{\mathbf{U}}_{j,k} = -\frac{1}{\Delta x} [\mathcal{F}_{j+\frac{1}{2},k} - \mathcal{F}_{j-\frac{1}{2},k}] - \frac{1}{\Delta y} [\mathcal{G}_{j,k+\frac{1}{2}} - \mathcal{G}_{j,k-\frac{1}{2}}],$$

with the following second-order numerical fluxes:

$$\mathcal{F}_{j+\frac{1}{2},k} = \mathbf{F}(\mathbf{U}_{j+\frac{1}{2},k}), \quad \mathbf{U}_{j+\frac{1}{2},k} := \mathbf{U}(\bar{\mathbf{V}}_{j+\frac{1}{2},k}^x) \quad \text{and} \quad \mathcal{G}_{j,k+\frac{1}{2}} = \mathbf{G}(\mathbf{U}_{j,k+\frac{1}{2}}), \quad \mathbf{U}_{j,k+\frac{1}{2}} := \mathbf{U}(\bar{\mathbf{V}}_{j,k+\frac{1}{2}}^y).$$

Two *independent* semi-discretizations of the nonconservative system (1.2) are obtained through the

modified 2-D PCCU scheme applied on the  $I_{j+\frac{1}{2},k}^x$  and  $I_{j,k+\frac{1}{2}}^y$  meshes, respectively, as follows:

$$\begin{aligned} \frac{d}{dt} \bar{\mathbf{V}}_{j+\frac{1}{2},k}^x = & -\frac{1}{\Delta x} \left[ \tilde{\mathcal{F}}_{j+1,k}^x - \tilde{\mathcal{F}}_{j,k}^x - \mathbf{B}_{j+\frac{1}{2},k}^x - \frac{a_{j,k}^{x,+}}{a_{j,k}^{x,+} - a_{j,k}^{x,-}} \mathbf{B}_{\Psi,j,k}^x + \frac{a_{j+1,k}^{x,-}}{a_{j+1,k}^{x,+} - a_{j+1,k}^{x,-}} \mathbf{B}_{\Psi,j+1,k}^x \right] \\ & - \frac{1}{\Delta y} \left[ \tilde{\mathcal{G}}_{j+\frac{1}{2},k+\frac{1}{2}}^x - \tilde{\mathcal{G}}_{j+\frac{1}{2},k-\frac{1}{2}}^x - \mathbf{C}_{j+\frac{1}{2},k}^x \right. \\ & \quad \left. - \frac{b_{j+\frac{1}{2},k-\frac{1}{2}}^{x,+}}{b_{j+\frac{1}{2},k-\frac{1}{2}}^{x,+} - b_{j+\frac{1}{2},k-\frac{1}{2}}^{x,-}} \mathbf{C}_{\Psi,j+\frac{1}{2},k-\frac{1}{2}}^x + \frac{b_{j+\frac{1}{2},k+\frac{1}{2}}^{x,-}}{b_{j+\frac{1}{2},k+\frac{1}{2}}^{x,+} - b_{j+\frac{1}{2},k+\frac{1}{2}}^{x,-}} \mathbf{C}_{\Psi,j+\frac{1}{2},k+\frac{1}{2}}^x \right] \end{aligned} \quad (3.1)$$

$$\begin{aligned} \frac{d}{dt} \bar{\mathbf{V}}_{j,k+\frac{1}{2}}^y = & -\frac{1}{\Delta x} \left[ \tilde{\mathcal{F}}_{j+\frac{1}{2},k+\frac{1}{2}}^y - \tilde{\mathcal{F}}_{j-\frac{1}{2},k+\frac{1}{2}}^y - \mathbf{B}_{j,k+\frac{1}{2}}^y \right. \\ & \quad \left. - \frac{a_{j-\frac{1}{2},k+\frac{1}{2}}^{y,+}}{a_{j-\frac{1}{2},k+\frac{1}{2}}^{y,+} - a_{j-\frac{1}{2},k+\frac{1}{2}}^{y,-}} \mathbf{B}_{\Psi,j-\frac{1}{2},k+\frac{1}{2}}^y + \frac{a_{j+\frac{1}{2},k+\frac{1}{2}}^{y,-}}{a_{j+\frac{1}{2},k+\frac{1}{2}}^{y,+} - a_{j+\frac{1}{2},k+\frac{1}{2}}^{y,-}} \mathbf{B}_{\Psi,j+\frac{1}{2},k+\frac{1}{2}}^y \right] \\ & - \frac{1}{\Delta y} \left[ \tilde{\mathcal{G}}_{j,k+1}^y - \tilde{\mathcal{G}}_{j,k}^y - \mathbf{C}_{j,k+\frac{1}{2}}^y \right. \\ & \quad \left. - \frac{b_{j,k}^{y,+}}{b_{j,k}^{y,+} - b_{j,k}^{y,-}} \mathbf{C}_{\Psi,j,k}^y + \frac{b_{j,k+1}^{y,-}}{b_{j,k+1}^{y,+} - b_{j,k+1}^{y,-}} \mathbf{C}_{\Psi,j,k+1}^y \right] \end{aligned} \quad (3.2)$$

Once again, we stress that the right-hand sides (RHSs) of (3.1) and (3.2) are computed independently and thus their computations can be performed in parallel.

The terms on the RHS of (3.1) are computed in a dimension-by-dimension manner and are given by

$$\begin{aligned} \tilde{\mathcal{F}}_{j,k}^x &= \frac{a_{j,k}^{x,+} \tilde{\mathbf{F}}(\mathbf{V}_{j,k}^{x,-}) - a_{j,k}^{x,-} \tilde{\mathbf{F}}(\mathbf{V}_{j,k}^{x,+})}{a_{j,k}^{x,+} - a_{j,k}^{x,-}} + \frac{a_{j,k}^{x,+} a_{j,k}^{x,-}}{a_{j,k}^{x,+} - a_{j,k}^{x,-} a} (\mathbf{V}_{j,k}^{x,+} - \mathbf{V}_{j,k}^{x,-} - \delta \mathbf{V}_{j,k}^x), \\ \delta \mathbf{V}_{j,k}^x &= \text{minmod}(\mathbf{V}_{j,k}^{x,*} - \mathbf{V}_{j,k}^{x,-}, \mathbf{V}_{j,k}^{x,+} - \mathbf{V}_{j,k}^{x,*}), \quad \mathbf{V}_{j,k}^{x,*} = \frac{a_{j,k}^{x,+} \mathbf{V}_{j,k}^{x,+} - a_{j,k}^{x,-} \mathbf{V}_{j,k}^{x,-} - \tilde{\mathbf{F}}(\mathbf{V}_{j,k}^{x,+}) + \tilde{\mathbf{F}}(\mathbf{V}_{j,k}^{x,-})}{a_{j,k}^{x,+} - a_{j,k}^{x,-}}, \\ \tilde{\mathcal{G}}_{j+\frac{1}{2},k+\frac{1}{2}}^x &= \frac{b_{j+\frac{1}{2},k+\frac{1}{2}}^{x,+} \tilde{\mathbf{G}}(\mathbf{V}_{j+\frac{1}{2},k+\frac{1}{2}}^{x,-}) - b_{j+\frac{1}{2},k+\frac{1}{2}}^{x,-} \tilde{\mathbf{G}}(\mathbf{V}_{j+\frac{1}{2},k+\frac{1}{2}}^{x,+})}{b_{j+\frac{1}{2},k+\frac{1}{2}}^{x,+} - b_{j+\frac{1}{2},k+\frac{1}{2}}^{x,-}} \\ &+ \frac{b_{j+\frac{1}{2},k+\frac{1}{2}}^{x,+} b_{j+\frac{1}{2},k+\frac{1}{2}}^{x,-}}{b_{j+\frac{1}{2},k+\frac{1}{2}}^{x,+} - b_{j+\frac{1}{2},k+\frac{1}{2}}^{x,-}} (\mathbf{V}_{j+\frac{1}{2},k+\frac{1}{2}}^{x,+} - \mathbf{V}_{j+\frac{1}{2},k+\frac{1}{2}}^{x,-} - \delta \mathbf{V}_{j+\frac{1}{2},k+\frac{1}{2}}^x), \\ \delta \mathbf{V}_{j+\frac{1}{2},k+\frac{1}{2}}^x &= \text{minmod}(\mathbf{V}_{j+\frac{1}{2},k+\frac{1}{2}}^{x,*} - \mathbf{V}_{j+\frac{1}{2},k+\frac{1}{2}}^{x,-}, \mathbf{V}_{j+\frac{1}{2},k+\frac{1}{2}}^{x,+} - \mathbf{V}_{j+\frac{1}{2},k+\frac{1}{2}}^{x,*}), \\ \mathbf{V}_{j+\frac{1}{2},k+\frac{1}{2}}^{x,*} &= \frac{b_{j+\frac{1}{2},k+\frac{1}{2}}^{x,+} \mathbf{V}_{j+\frac{1}{2},k+\frac{1}{2}}^{x,+} - b_{j+\frac{1}{2},k+\frac{1}{2}}^{x,-} \mathbf{V}_{j+\frac{1}{2},k+\frac{1}{2}}^{x,-} - \tilde{\mathbf{G}}(\mathbf{V}_{j+\frac{1}{2},k+\frac{1}{2}}^{x,+}) + \tilde{\mathbf{G}}(\mathbf{V}_{j+\frac{1}{2},k+\frac{1}{2}}^{x,-})}{b_{j+\frac{1}{2},k+\frac{1}{2}}^{x,+} - b_{j+\frac{1}{2},k+\frac{1}{2}}^{x,-}}, \\ \mathbf{B}_{j+\frac{1}{2},k}^x &= B(\bar{\mathbf{V}}_{j+\frac{1}{2},k}^x)(\mathbf{V}_{j+1,k}^{x,-} - \mathbf{V}_{j,k}^{x,+}), \\ \mathbf{B}_{\Psi,j,k}^x &= \frac{1}{2} [B(\mathbf{V}_{j,k}^{x,-}) + B(\mathbf{V}_{j,k}^{x,+})](\mathbf{V}_{j,k}^{x,+} - \mathbf{V}_{j,k}^{x,-}), \\ \mathbf{C}_{j+\frac{1}{2},k}^x &= C(\bar{\mathbf{V}}_{j+\frac{1}{2},k}^x)(\mathbf{V}_{j+\frac{1}{2},k+\frac{1}{2}}^{x,-} - \mathbf{V}_{j+\frac{1}{2},k-\frac{1}{2}}^{x,+}), \\ \mathbf{C}_{\Psi,j+\frac{1}{2},k+\frac{1}{2}}^x &= \frac{1}{2} [C(\mathbf{V}_{j+\frac{1}{2},k+\frac{1}{2}}^{x,-}) + C(\mathbf{V}_{j+\frac{1}{2},k+\frac{1}{2}}^{x,+})](\mathbf{V}_{j+\frac{1}{2},k+\frac{1}{2}}^{x,+} - \mathbf{V}_{j+\frac{1}{2},k+\frac{1}{2}}^{x,-}), \end{aligned}$$

where  $\mathbf{V}_{j,k}^{x,+}$  and  $\mathbf{V}_{j+\frac{1}{2},k+\frac{1}{2}}^{x,+}$  are reconstructed point values obtained from the cell averages  $\{\bar{\mathbf{V}}_{j,k}^x\}$ . As in the 1-D case, we compute these values by exploiting the local characteristic decomposition. In the  $x$ -direction, we have

$$\mathbf{V}_{j,k}^{x,+} = Q_{j+\frac{1}{2},k}^x \Gamma_{j,k}^{x,+}, \quad \mathbf{V}_{j+1,k}^{x,-} = Q_{j+\frac{1}{2},k}^x \Gamma_{j+1,k}^{x,-},$$

where

$$\Gamma_{j,k}^{x,+} = \Gamma_{j+\frac{1}{2},k}^x - \frac{\Delta x}{2} (\Gamma_x)_{j+\frac{1}{2},k}^x, \quad \Gamma_{j+1,k}^{x,-} = \Gamma_{j+\frac{1}{2},k}^x + \frac{\Delta x}{2} (\Gamma_x)_{j+\frac{1}{2},k}^x$$

with the slopes computed using the generalized minmod limiter:

$$(\Gamma_x)_{j+\frac{1}{2},k}^x = \text{minmod} \left( \theta \frac{\Gamma_{j+\frac{1}{2},k}^x - \Gamma_{j-\frac{1}{2},k}^x}{\Delta x}, \frac{\Gamma_{j+\frac{3}{2},k}^x - \Gamma_{j-\frac{1}{2},k}^x}{2\Delta x}, \theta \frac{\Gamma_{j+\frac{3}{2},k}^x - \Gamma_{j+\frac{1}{2},k}^x}{\Delta x} \right), \quad \theta \in [0, 1]. \quad (3.3)$$

In (3.3), one has

$$\Gamma_{j-\frac{1}{2},k}^x = (Q_{j+\frac{1}{2},k}^x)^{-1} \bar{\mathbf{V}}_{j-\frac{1}{2},k}^x, \quad \Gamma_{j+\frac{1}{2},k}^x = (Q_{j+\frac{1}{2},k}^x)^{-1} \bar{\mathbf{V}}_{j+\frac{1}{2},k}^x, \quad \Gamma_{j+\frac{3}{2},k}^x = (Q_{j+\frac{1}{2},k}^x)^{-1} \bar{\mathbf{V}}_{j+\frac{3}{2},k}^x,$$

where the matrix  $Q_{j+\frac{1}{2},k}^x$  is such that  $(Q_{j+\frac{1}{2},k}^x)^{-1} \mathcal{A}_{j+\frac{1}{2},k}^x Q_{j+\frac{1}{2},k}^x$  is diagonal with  $\mathcal{A}_{j+\frac{1}{2},k}^x = \mathcal{A}(\bar{\mathbf{V}}_{j+\frac{1}{2},k}^x) := \frac{\partial \tilde{F}}{\partial \mathbf{V}}(\bar{\mathbf{V}}_{j+\frac{1}{2},k}^x) - B(\bar{\mathbf{V}}_{j+\frac{1}{2},k}^x)$ .

Similarly, in the  $y$ -direction, we have

$$\mathbf{V}_{j+\frac{1}{2},k-\frac{1}{2}}^{x,+} = P_{j+\frac{1}{2},k}^x \Gamma_{j+\frac{1}{2},k-\frac{1}{2}}^{x,+}, \quad \mathbf{V}_{j+\frac{1}{2},k+\frac{1}{2}}^{x,-} = P_{j+\frac{1}{2},k}^x \Gamma_{j+\frac{1}{2},k+\frac{1}{2}}^{x,-},$$

where

$$\Gamma_{j+\frac{1}{2},k-\frac{1}{2}}^{x,+} = \Gamma_{j+\frac{1}{2},k}^y - \frac{\Delta y}{2} (\Gamma_y)_{j+\frac{1}{2},k}^y, \quad \Gamma_{j+\frac{1}{2},k+\frac{1}{2}}^{x,-} = \Gamma_{j+\frac{1}{2},k}^y + \frac{\Delta y}{2} (\Gamma_y)_{j+\frac{1}{2},k}^y$$

with the slope given by

$$(\Gamma_y)_{j+\frac{1}{2},k}^x = \text{minmod} \left( \theta \frac{\Gamma_{j+\frac{1}{2},k}^x - \Gamma_{j+\frac{1}{2},k-1}^x}{\Delta y}, \frac{\Gamma_{j+\frac{1}{2},k+1}^x - \Gamma_{j+\frac{1}{2},k-1}^x}{2\Delta y}, \theta \frac{\Gamma_{j+\frac{1}{2},k+1}^x - \Gamma_{j+\frac{1}{2},k}^x}{\Delta y} \right), \quad \theta \in [0, 1]. \quad (3.4)$$

In (3.4), one has

$$\Gamma_{j+\frac{1}{2},k-1}^x = (P_{j+\frac{1}{2},k}^x)^{-1} \bar{\mathbf{V}}_{j+\frac{1}{2},k-1}^x, \quad \Gamma_{j+\frac{1}{2},k}^x = (P_{j+\frac{1}{2},k}^x)^{-1} \bar{\mathbf{V}}_{j+\frac{1}{2},k}^x, \quad \Gamma_{j+\frac{1}{2},k+1}^x = (P_{j+\frac{1}{2},k}^x)^{-1} \bar{\mathbf{V}}_{j+\frac{1}{2},k+1}^x,$$

where the matrix  $P_{j+\frac{1}{2},k}^x$  is such that  $(P_{j+\frac{1}{2},k}^x)^{-1} \mathcal{B}_{j+\frac{1}{2},k}^x P_{j+\frac{1}{2},k}^x$  is diagonal with  $\mathcal{B}_{j+\frac{1}{2},k}^x = \mathcal{B}(\bar{\mathbf{V}}_{j+\frac{1}{2},k}^x) := \frac{\partial \tilde{G}}{\partial \mathbf{V}}(\bar{\mathbf{V}}_{j+\frac{1}{2},k}^x) - C(\bar{\mathbf{V}}_{j+\frac{1}{2},k}^x)$ .

The one-sided local speeds of propagation in (3.1) are estimated by

$$\begin{aligned} a_{j,k}^{x,-} &= \min \{ \lambda_1(\mathbf{V}_{j,k}^{x,-}), \lambda_1(\mathbf{V}_{j,k}^{x,+}), 0 \}, & a_{j,k}^{x,+} &= \max \{ \lambda_M(\mathbf{V}_{j,k}^{x,-}), \lambda_M(\mathbf{V}_{j,k}^{x,+}), 0 \}, \\ b_{j+\frac{1}{2},k+\frac{1}{2}}^{x,-} &= \min \{ \mu_1(\mathbf{V}_{j+\frac{1}{2},k+\frac{1}{2}}^{x,-}), \mu_1(\mathbf{V}_{j+\frac{1}{2},k+\frac{1}{2}}^{x,+}), 0 \}, & b_{j+\frac{1}{2},k+\frac{1}{2}}^{x,+} &= \max \{ \mu_M(\mathbf{V}_{j+\frac{1}{2},k+\frac{1}{2}}^{x,-}), \mu_M(\mathbf{V}_{j+\frac{1}{2},k+\frac{1}{2}}^{x,+}), 0 \}, \end{aligned}$$

where  $\lambda_1(\mathbf{V}) \leq \dots \leq \lambda_M(\mathbf{V})$  are the eigenvalues of  $\mathcal{A}(\mathbf{V})$  and  $\mu_1(\mathbf{V}) \leq \dots \leq \mu_M(\mathbf{V})$  are the eigenvalues of  $\mathcal{B}(\mathbf{V})$ .

The terms on the RHS of (3.2), related to the update of  $\bar{\mathbf{V}}_{j,k+\frac{1}{2}}^y$ , can be analogously computed through the same formulae used to evaluate the RHS of (3.1), but with the first index shifted by  $-\frac{1}{2}$ , the second index shifted by  $+\frac{1}{2}$ , and the superscripts “ $x$ ” replaced by “ $y$ ”.

**Remark 3.1** We would like to emphasize that, as in the 1-D case, the proposed 2-D DF-FV method is not tied to the PCCU scheme and the nonconservative system (1.2) can be numerically solved by an alternative second-order stable numerical method.

Finally, the post-processing is carried out in a “dimension-by-dimension” manner by alternating sweeps in the  $x$ -direction, in which we modify the cell averages of  $\bar{U}$  and  $\bar{V}^x$ , and in the  $y$ -direction, in which we modify the cell averages of  $\bar{U}$  and  $\bar{V}^y$ . There are two straightforward implementation options: first, to perform the sweep in the  $x$ -direction and then the one in the  $y$ -direction, or the other way around. Unfortunately, both of these options may lead to asymmetries with respect to the two Cartesian directions. To prevent this, we average the results given by these two alternatives. Namely, using the same notation as in the 1-D case, we start from  $\{\bar{U}_{j,k}^*\}$ ,  $\{\bar{V}_{j+\frac{1}{2},k}^{x,*}\}$ , and  $\{\bar{V}_{j,k+\frac{1}{2}}^{y,*}\}$ , denoting the solution values evolved from time  $t$  to  $t + \Delta t$  by an ODE solver, and we independently perform two sub-post-processings:

- One with the sweeps in the  $x$ - and then  $y$ -direction, resulting in  $\{\bar{U}_{j,k}^{xy}\}$ ,  $\{\bar{V}_{j+\frac{1}{2},k}^{x,xy}\}$ , and  $\{\bar{V}_{j,k+\frac{1}{2}}^{y,xy}\}$ ;
- The other one with the sweeps in the  $y$ - and then  $x$ -direction, resulting in  $\{\bar{U}_{j,k}^{yx}\}$ ,  $\{\bar{V}_{j+\frac{1}{2},k}^{x,yx}\}$ , and  $\{\bar{V}_{j,k+\frac{1}{2}}^{y,yx}\}$ .

Upon the completion of these two sub-post-processing steps, we set

$$\begin{aligned}\bar{U}_{j,k}(t + \Delta t) &= \frac{1}{2}(\bar{U}_{j,k}^{xy} + \bar{U}_{j,k}^{yx}), \\ \bar{V}_{j+\frac{1}{2},k}^x(t + \Delta t) &= \frac{1}{2}(\bar{V}_{j+\frac{1}{2},k}^{x,xy} + \bar{V}_{j+\frac{1}{2},k}^{y,yx}), \quad \bar{V}_{j,k+\frac{1}{2}}^y(t + \Delta t) = \frac{1}{2}(\bar{V}_{j,k+\frac{1}{2}}^{y,xy} + \bar{V}_{j,k+\frac{1}{2}}^{x,yx}).\end{aligned}$$

The first of the proposed sub-post-processings can be presented algorithmically through the following eight steps, with Steps 1–4 corresponding to the sweep in the  $x$ -direction and Steps 5–8 corresponding to the sweep in the  $y$ -direction.

**Step 1.** Compute the conserved variables at  $(x_{j+\frac{1}{2}}, y_k)$  using the transformation from the primitive ones:

$$\mathbf{U}_{j+\frac{1}{2},k}^* = \mathbf{U}(\bar{V}_{j+\frac{1}{2},k}^{x,*}).$$

**Step 2.** Perform the piecewise linear reconstruction for  $\mathbf{U}$  in the  $x$ -direction using the slopes computed by the minmod limiter

$$(\mathbf{U}_x)_{j,k}^* = 2 \text{minmod} \left( \frac{\bar{U}_{j,k}^* - \bar{U}_{j-\frac{1}{2},k}^*}{\Delta x}, \frac{\bar{U}_{j+\frac{1}{2},k}^* - \bar{U}_{j,k}^*}{\Delta x} \right),$$

which results in

$$\mathbf{U}_{j+\frac{1}{2},k}^{*,-} := \bar{U}_{j,k}^* + \frac{\Delta x}{2}(\mathbf{U}_x)_{j,k}^*, \quad \mathbf{U}_{j+\frac{1}{2},k}^{*,+} := \bar{U}_{j+1,k}^* - \frac{\Delta x}{2}(\mathbf{U}_x)_{j+1,k}^*.$$

**Step 3.** Set

$$\mathbf{U}_{j+\frac{1}{2},k}^{**} := \frac{1}{2}(\mathbf{U}_{j+\frac{1}{2},k}^{*,-} + \mathbf{U}_{j+\frac{1}{2},k}^{*,+}),$$

and recompute the primitive variables at  $(x_{j+\frac{1}{2}}, y_k)$  using the transformation from the conservative ones:

$$\bar{V}_{j+\frac{1}{2},k}^{x,xy} = \mathbf{V}(\mathbf{U}_{j+\frac{1}{2},k}^{**}).$$

**Step 4.** Correct the conserved variables by setting

$$\tilde{\mathbf{U}}_{j,k} := \frac{1}{2}(\mathbf{U}_{j-\frac{1}{2},k}^{**} + \mathbf{U}_{j+\frac{1}{2},k}^{**}).$$

**Step 5.** Compute the conserved variables at  $(x_j, y_{k+\frac{1}{2}})$  using the transformation from the primitive ones:

$$\mathbf{U}_{j,k+\frac{1}{2}}^* = \mathbf{U}(\bar{\mathbf{V}}_{j,k+\frac{1}{2}}^{y,*}).$$

**Step 6.** Perform the piecewise linear reconstruction for  $\mathbf{U}$  in the  $y$ -direction using the slopes computed by the minmod limiter

$$(\mathbf{U}_y)_{j,k}^* = 2 \text{minmod} \left( \frac{\bar{\mathbf{U}}_{j,k} - \mathbf{U}_{j,k-\frac{1}{2}}^*}{\Delta y}, \frac{\mathbf{U}_{j,k+\frac{1}{2}}^* - \bar{\mathbf{U}}_{j,k}}{\Delta y} \right),$$

which results in

$$\mathbf{U}_{j,k+\frac{1}{2}}^{*,-} := \bar{\mathbf{U}}_{j,k} + \frac{\Delta y}{2} (\mathbf{U}_y)_{j,k}^*, \quad \mathbf{U}_{j,k-\frac{1}{2}}^{*,+} := \bar{\mathbf{U}}_{j,k+1}^* - \frac{\Delta y}{2} (\mathbf{U}_y)_{j,k+1}^*.$$

**Step 7.** Set

$$\mathbf{U}_{j,k+\frac{1}{2}}^{**} := \frac{1}{2} (\mathbf{U}_{j,k+\frac{1}{2}}^{*,-} + \mathbf{U}_{j,k+\frac{1}{2}}^{*,+}),$$

and recompute the primitive variables at  $(x_j, y_{k+\frac{1}{2}})$  using the transformation from the conservative ones:

$$\bar{\mathbf{V}}_{j,k+\frac{1}{2}}^{y,xy} = \mathbf{V}(\mathbf{U}_{j,k+\frac{1}{2}}^{**}).$$

**Step 8.** Correct the conserved variables by setting

$$\bar{\mathbf{U}}_{j,k}^{xy} = \frac{1}{2} (\mathbf{U}_{j,k-\frac{1}{2}}^{**} + \mathbf{U}_{j,k+\frac{1}{2}}^{**}).$$

**Remark 3.2** We would like to stress that many operations within the proposed DF-FV method can be carried out in parallel. The updates of  $\mathbf{V}^x$  and  $\mathbf{V}^y$  can be performed independently, while, the update of  $\mathbf{U}$  requires  $\mathbf{V}^x$  and  $\mathbf{V}^y$ , but no reconstructions and simple numerical flux evaluations. Therefore, with a suitable parallelization of the operations, the computational cost may be significantly reduced, especially since the post-processing is performed only once per time step.

## 4 Numerical Examples

In this section, we present the numerical results obtained for the Euler equations of gas dynamics. In the 1-D case, these equations can be written in either the conservative form (2.1) with

$$\mathbf{U} = (\rho, \rho u, E)^\top, \quad \mathbf{F}(\mathbf{U}) = (\rho u, \rho u^2 + p, u(E + p))^\top,$$

and the equation of state  $E = \frac{p}{\gamma-1} + \frac{1}{2}\rho u^2$ , or the nonconservative form (2.2) with

$$\mathbf{V} = (\rho, u, p)^\top, \quad \tilde{\mathbf{F}}(\mathbf{V}) = \left( \rho u, \frac{u^2}{2}, pu \right)^\top, \quad \mathbf{B}(\mathbf{V}) = \begin{pmatrix} 0 & 0 & 0 \\ 0 & 0 & -\frac{1}{\rho} \\ 0 & -(\gamma-1)p & 0 \end{pmatrix}.$$

In all of the numerical examples below, the time discretization is performed using the three-stage third-order strong stability-preserving Runge-Kutta (SSPRK3) method (see, e.g., [20,21]) with the time-step selected adaptively with the CFL number set to be 0.475. We remark that one can replace the

SSPRK3 ODE solver with one's favourite alternative. Our selection is motivated by the good stability properties of the SSPRK3 method.

The minmod parameter has been set to  $\theta = 1.3$  in all examples except Example 5, where  $\theta = 1.1$  was used. In all of the examples, we set  $\gamma = 1.4$ .

In Examples 2–5, we also compare the performance of the proposed DF-FV method with the second-order central scheme on overlapping cells (CSOC) from [31], implemented on the same mesh as the DF-FV method.

**Example 1 (accuracy test for unsteady isentropic vortex).** In the first example taken from [5, 35, 43], we numerically verify the accuracy of the proposed DF-FV method.

We consider a smooth unsteady vortex on the computational domain  $[-10, 10] \times [-10, 10]$ , endowed with periodic boundary conditions. The initial data are

$$\begin{aligned}\rho(x, y, 0) &= \left(1 - \frac{(\gamma - 1)\kappa^2}{2\gamma}\right)^{\frac{1}{\gamma-1}}, \quad p(x, y, 0) = \rho^\gamma(x, y, 0), \\ u(x, y, 0) &= 1 - \kappa y, \quad v(x, y, 0) = 1 + \kappa x, \quad \kappa = \frac{5}{2\pi} e^{\frac{1-x^2-y^2}{2}}.\end{aligned}$$

The exact solution is given by  $\mathbf{U}(x, y, t) = \mathbf{U}(x - t, y - t, 0)$ , modulo the periodic boundary conditions.

We compute the solution until the final time  $t = 0.1$  on a sequence of uniform  $N \times N$  meshes with  $N = 100, 200, 400, 800$ , and  $1600$ . The obtained results are reported in Table 4.1, in which we demonstrate that the expected order of convergence is achieved in the  $\mathbf{U}$ -solution (we show the  $\rho$ -,  $\rho u$ -, and  $E$ -components),  $\mathbf{V}^x$ -solution (we show the  $v$ -component), and  $\mathbf{V}^y$ -solution (we show the  $p$ -component). The same order is observed in all other components, not shown here for the sake of brevity.

$N$	$\rho$ -error	rate	$\rho u$ -error	rate	$E$ -error	rate	$v$ -error	rate	$p$ -error	rate
100	1.08e-2	—	2.59e-2	—	6.36e-2	—	6.15e-2	—	3.33e-2	—
200	3.04e-3	1.82	6.44e-3	2.01	1.66e-2	1.94	1.58e-2	1.96	7.91e-3	2.07
400	9.08e-4	1.74	1.68e-3	1.94	4.38e-3	1.93	4.12e-3	1.94	1.90e-3	2.06
800	2.44e-4	1.90	4.25e-4	1.98	1.08e-3	2.01	1.04e-3	1.99	4.53e-4	2.07
1600	5.86e-5	2.06	1.01e-4	2.07	2.44e-4	2.15	2.56e-4	2.02	1.06e-4	2.10

Table 4.1: Example 1:  $L^1$ -errors and corresponding convergence rates for the  $\rho$ -,  $\rho u$ -, and  $E$ -components of the  $\mathbf{U}$ -solution,  $v$ -component of the  $\mathbf{V}^x$ -solution, and  $p$ -component of the  $\mathbf{V}^y$ -solution.

It should be observed that in this example, the solution is smooth and thus it can, in principle, be computed without post-processing. We have verified that, in this case, the second-order convergence is also achieved. These results are, however, omitted since the presented DF-FV method without the post-processing is impractical.

**Example 2 (Sod shock-tube problem).** In the second example, we consider the Sod shock-tube problem from [45]. The Riemann initial data,

$$\mathbf{V}(x, 0) = \begin{cases} (1, 0, 1)^\top, & x < 0.5, \\ (0.125, 0, 0.1)^\top, & \text{otherwise,} \end{cases}$$

are prescribed in the computational domain  $[0, 1]$  with the free boundary conditions.

We compute the solution until the final time  $t = 0.2$  on a uniform mesh with  $N = 200$  and plot it in Figure 4.1 together with the exact solution, obtained using the library NUMERICA [47], and the solution computed by the DF-FV method but without post-processing. As one can see, the DF-FV solution is oscillation-free and its rather sharply resolved discontinuities are located at the correct locations thanks to the conservative post-processing. On the contrary, the DF-FV method without the post-processing produces very large spurious spikes in the  $\mathbf{U}$ -solution (note that these spikes are located exactly where the initial condition was discontinuous) and a non-oscillatory  $\mathbf{V}$ -solution, which apparently captures a wrong weak solution as expected (see [3, 23]). Therefore, using such  $\mathbf{V}$ -values to update the  $\mathbf{U}$ -variables prevents convergence to the correct weak solution, despite the conservative nature of the update. In fact, refining the mesh does not lead to convergence of the  $\mathbf{U}$  solution, and the spurious spikes persist without decay.

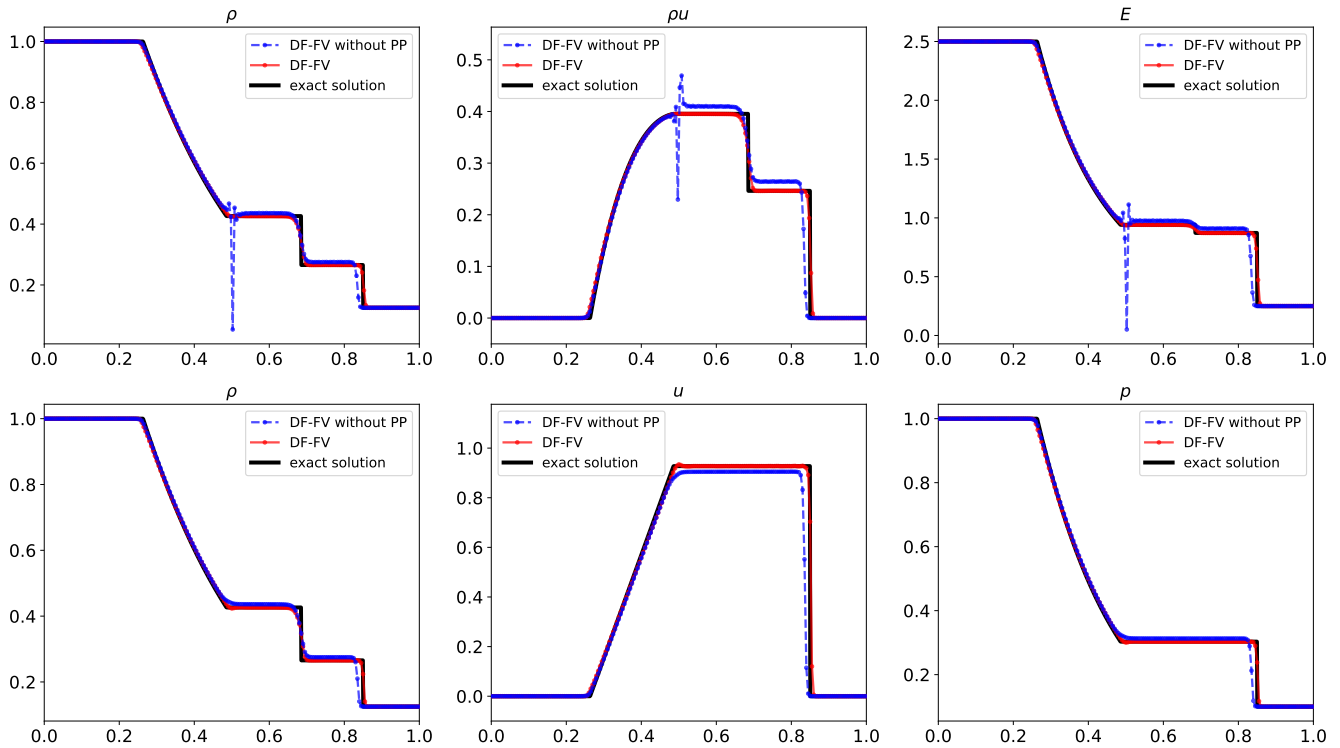


Figure 4.1: Example 2:  $\mathbf{U}$ -solutions (upper row) and  $\mathbf{V}$ -solutions (lower row) computed by the DF-FV method and the DF-FV method without the post-processing.

In Figure 4.2, we report the comparison between the DF-FV method and CSOC. While the results are comparable, one can see that the DF-FV method slightly outperforms its counterpart even on this very basic numerical example.

**Example 3 (double rarefaction problem).** In this problem taken from [48], we consider a Riemann problem, whose solution contains two rarefaction waves, which expand and form a near-vacuum area in the middle of the computational domain  $[0, 1]$ . The initial conditions,

$$\mathbf{V}(x, 0) = \begin{cases} (1, -2, 0.4)^T, & x < 0.5, \\ (1, 2, 0.4)^T, & \text{otherwise,} \end{cases}$$

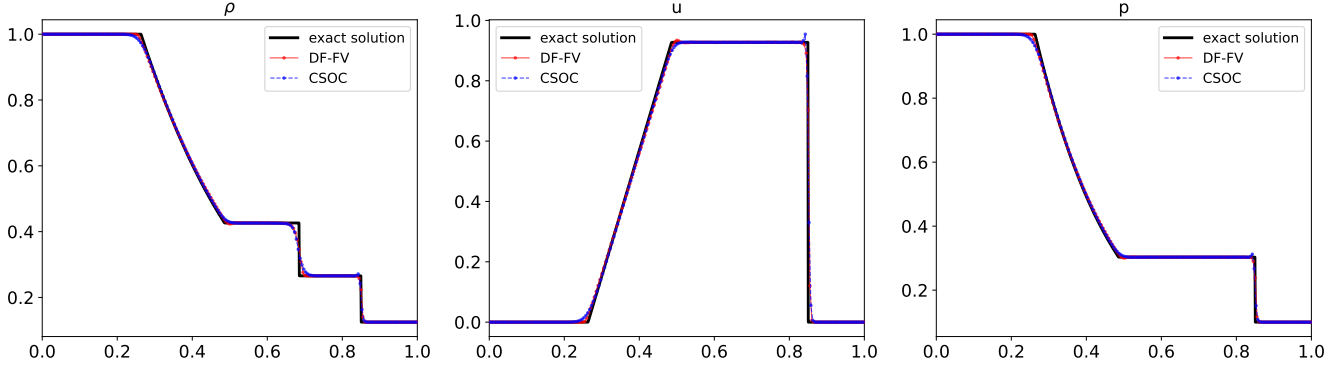


Figure 4.2: Example 2: Comparison between the DF-FV  $V$ -solution and CSOC solution.

are supplemented with the free boundary conditions.

We compute the solution by the DF-FV method and CSOC until the final time  $t = 0.15$  on a uniform mesh with  $N = 200$  and plot the obtained results together with the exact solution, once again generated using the library NUMERICA [47] in Figure 4.3. As one can see, both schemes preserve the positivity of the density and pressure and the obtained solutions are oscillation-free. At the same time, the proposed DF-FV method outperforms the CSOC in the resolution of low-density parts of the computed solutions and near the rarefaction corners even though the enlarged numerical diffusion attributed to the post-processing oversmears the velocity profile captured by the DF-FV method.

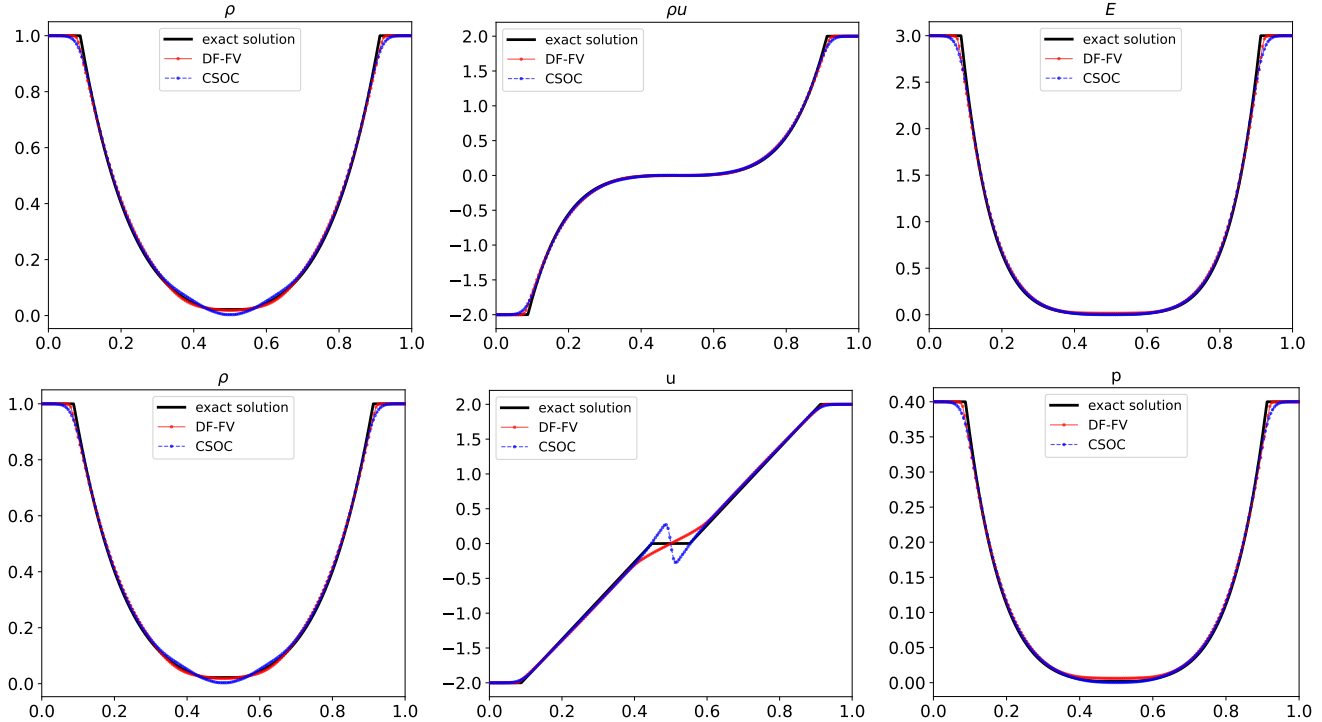


Figure 4.3: Example 3:  $U$ -solutions (upper row) and  $V$ -solutions (lower row) plotted along with the CSOC solution.

**Example 4 (shock-turbulence interaction problem).** In this example taken from [44], a shock interacts with a turbulent flow characterized by high-frequency oscillations.

The initial data,

$$\mathbf{V}(x, 0) = \begin{cases} (3.857143, 2.629369, 10.333333)^T, & x < -4, \\ (1 + 0.2 \sin(5x), 0, 1)^T, & \text{otherwise,} \end{cases}$$

are prescribed in the computational domain  $[-5, 5]$  with the inflow boundary conditions at the left boundary and free boundary conditions at the right one.

We compute the solution by the DF-FV method and CSOC until the final time  $t = 1.8$  on a uniform mesh with  $N = 600$  and report the obtained results in Figure 4.4. Since in this example no exact solution is available, we compute the reference solution by a second-order semi-discrete CU scheme from [24] on a much finer uniform mesh consisting of 200000 cells. As one can see, the solution structures are correctly resolved by both of the studied schemes, but the resolution of the smooth, oscillating parts of the solution achieved by the DF-FV method is substantially higher, as can be further seen in Figure 4.5, where a zoom at the spatial interval  $[0, 2.5]$  is shown.

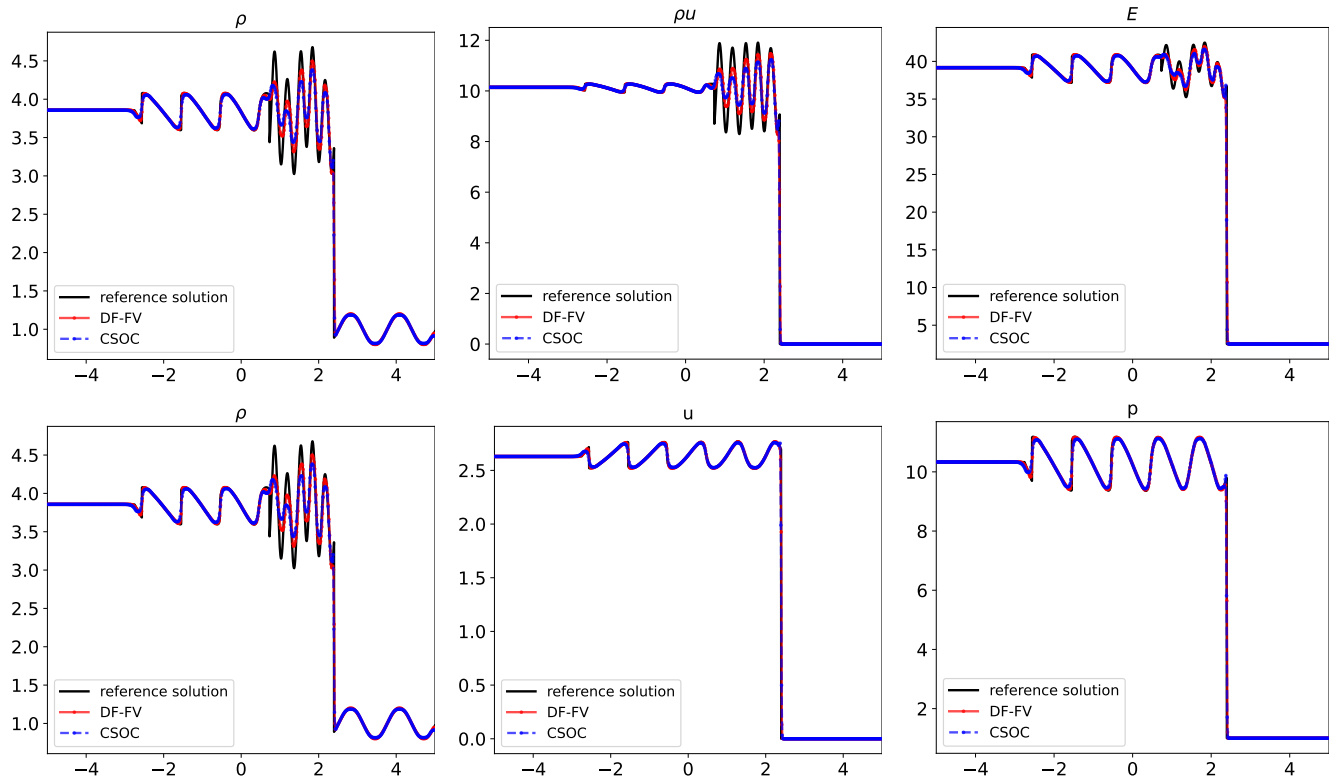


Figure 4.4: Example 4:  $\mathbf{U}$ -solutions (upper row) and  $\mathbf{V}$ -solutions (lower row) plotted along with the CSOC solution.

**Example 5 (Woodward-Colella problem).** In this problem, which was introduced in [49], the initial conditions,

$$\mathbf{V}(x, 0) = \begin{cases} (1, 0, 10^3)^T, & x < 0.1, \\ (1, 0, 10^2)^T, & x > 0.9, \\ (1, 0, 10^{-2})^T, & \text{otherwise,} \end{cases}$$

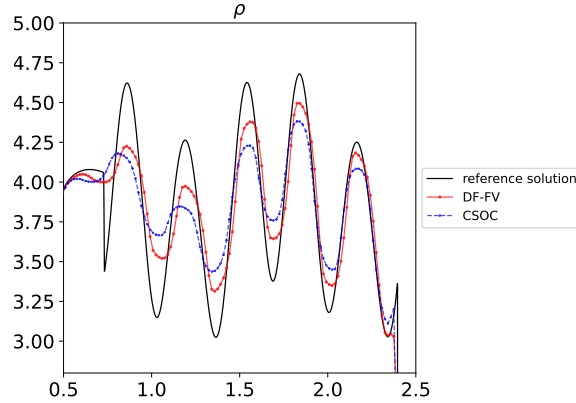


Figure 4.5: The same as in the upper left panel in Figure 4.4, but zoomed at  $x \in [0, 2.5]$ .

are prescribed in the computational domain  $[0, 1]$  with solid wall boundary conditions.

In Figure 4.6, we plot the solutions computed by the DF-FV method and CSOC at the final time  $t = 0.038$  on a uniform mesh with  $N = 400$  along with the reference solution generated by a second-order semi-discrete CU scheme from [24] with reconstruction of characteristic variables and the same time discretization on a much finer uniform mesh consisting of 200000 cells. The obtained results demonstrate the ability of the proposed DF-FV method to capture strong discontinuities. It also clearly shows the superiority of our method compared to the CSOC.

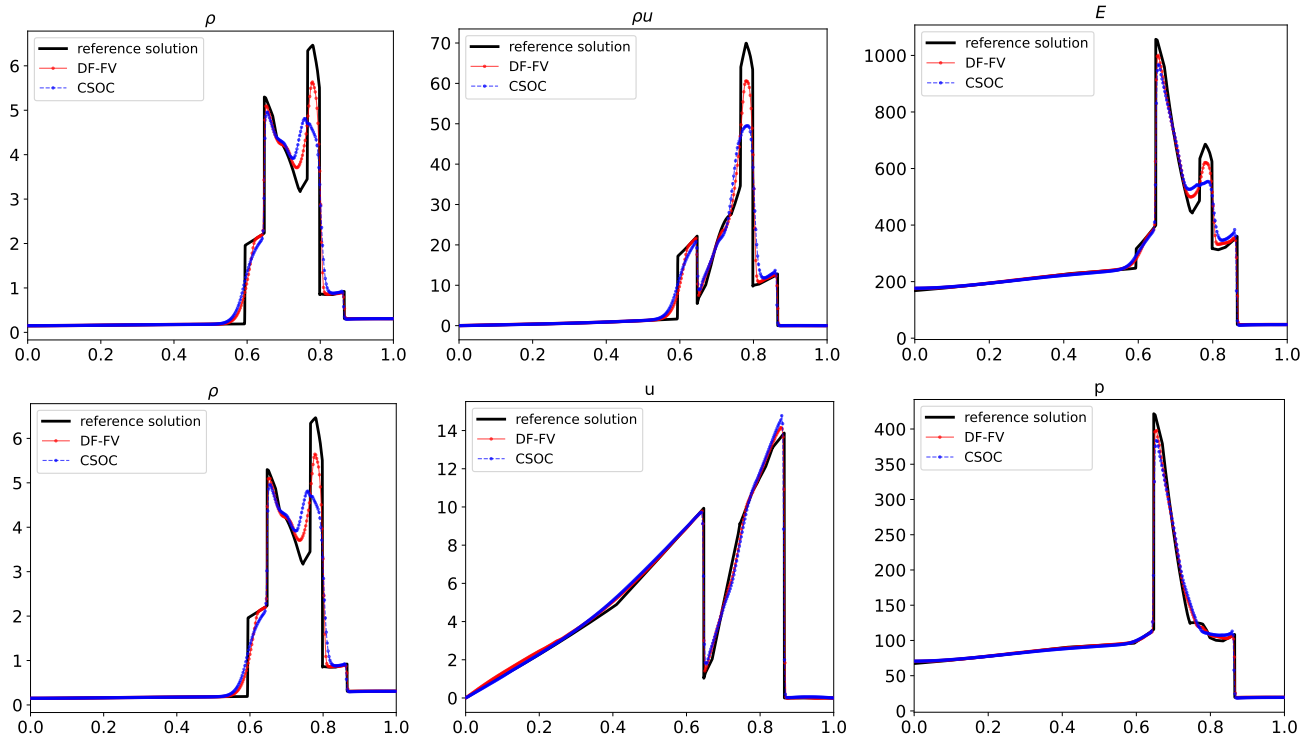


Figure 4.6: Example 5:  $U$ -solutions (upper row) and  $V$ -solutions (lower row) plotted along with the CSOC solution.

**Example 6 (explosion problem).** This problem, taken from [48], is a multidimensional extension of the Sod shock-tube problem considered in Example 2.

We take the following initial conditions:

$$\mathbf{V}(x, y, 0) = \begin{cases} (1, 0, 0, 1)^\top, & \sqrt{x^2 + y^2} < 0.4, \\ (0.125, 0, 0, 0.1)^\top, & \text{otherwise,} \end{cases}$$

which are prescribed in the computational domain  $[-1, 1] \times [-1, 1]$  with the free boundary conditions.

We compute the solution until the final time  $t = 0.25$  on a uniform mesh with  $N_x = N_y = 400$ . In Figure 4.7, we report three-dimensional plots of the density- and energy-components of the  $\mathbf{U}$ -solution and the density- and pressure-components of the  $\mathbf{V}^x$ -solution (we do not show the  $\mathbf{V}^y$ -solution as it is practically the same as the  $\mathbf{V}^x$ -one). The 1-D slices of  $\rho$ ,  $\sqrt{(\rho u)^2 + (\rho v)^2}$ , and  $E$  from the  $\mathbf{U}$ -solution and of  $\rho$ ,  $\sqrt{u^2 + v^2}$ , and  $p$  from the  $\mathbf{V}^x$ -solution along the line  $y = x$  are shown in Figure 4.8 (the reference solution plotted there has been obtained by a second-order semi-discrete FV scheme with reconstruction of characteristic variables and exact Riemann solver numerical flux on a much finer uniform mesh consisting of  $3000 \times 3000$  cells). As one can see, the numerical solution does not exhibit significant spurious oscillations or anomalous features, and the solution is sharply captured. One can also observe that the radial symmetry is preserved.

**Example 7 (shock-vortex interaction).** In this test, which was studied in, e.g., [15, 18, 41], we consider a moving vortex with Mach number  $M_v := 0.9$  interacting with a stationary shock with Mach number  $M_s := 1.5$ . Such an interaction gives rise to complex flow structures, making this numerical test challenging for higher-order numerical schemes.

A schematic of the initial setup is shown in Figure 4.9. Specifically, the computational domain  $[0, 2] \times [0, 1]$  is divided into two main subdomains by the vertical line  $x = 0.5$ . The vortex is initially located within a circular area centered on  $(x_c, y_c) := (0.25, 0.5)$  and occupies regions I and II: the first one is a circle of radius  $a = 0.075$  and the latter one is a concentrical annulus with inner radius  $a$  and outer radius  $b = 0.175$ . The states in regions III and IV correspond to a stationary shock. In particular, given the left constant state from region III,

$$\rho_{\text{III}} = 1, \quad u_{\text{III}} = \sqrt{\gamma} M_s, \quad v_{\text{III}} = 0, \quad p_{\text{III}} = 1,$$

the right state,  $(\rho_{\text{IV}}, u_{\text{IV}}, v_{\text{IV}}, p_{\text{IV}})$ , can be easily computed through the Rankine-Hugoniot conditions (see [48, Section 3.1.3]), leading to

$$\rho_{\text{IV}} = \frac{(\gamma + 1)M_s^2}{(\gamma - 1)M_s^2 + 2}\rho_{\text{III}}, \quad u_{\text{IV}} = \frac{(\gamma - 1)M_s^2 + 2}{(\gamma + 1)M_s^2}u_{\text{III}}, \quad v_{\text{IV}} = 0, \quad p_{\text{IV}} = \frac{2\gamma M_s^2 - (\gamma - 1)}{\gamma + 1}p_{\text{III}}.$$

The velocity profile in vortex regions I and II is given, in terms of radial coordinates  $(r, \vartheta)$  with respect to the center  $(x_c, y_c)$ :

$$u(r, \vartheta) = u_{\text{III}} - v_\vartheta \sin \vartheta, \quad v(r, \vartheta) = v_{\text{III}} + v_\vartheta \cos \vartheta,$$

where

$$v_\vartheta := \begin{cases} v_m \frac{r}{a}, & r \leq a, \\ v_m \frac{a}{a^2 - b^2} \left( r - \frac{b^2}{r} \right), & a < r < b, \\ 0, & r \geq b, \end{cases}$$

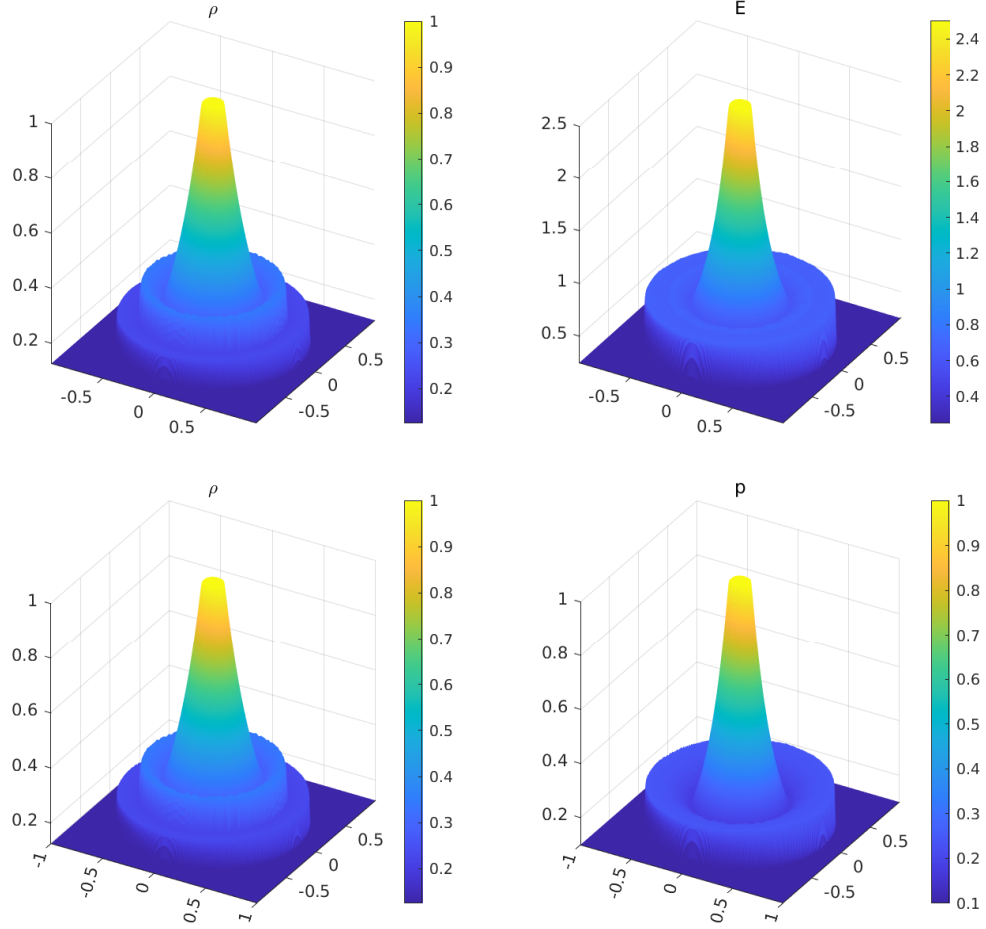


Figure 4.7: Example 6: Density- and energy-components of the  $U$ -solution (upper row) and density- and pressure-components of the  $V^x$ -solution (lower row).

with  $v_m := M_v \sqrt{\gamma}$  being the maximal angular velocity.

Density and pressure profiles inside the vortex are obtained by imposing a balance between centripetal force and pressure gradients [41], resulting in

$$p = p_{\text{III}} \left( \frac{T}{T_{\text{III}}} \right)^{\frac{\gamma}{\gamma-1}}, \quad \rho = \rho_{\text{III}} \left( \frac{T}{T_{\text{III}}} \right)^{\frac{1}{\gamma-1}},$$

where  $T_{\text{III}} = \frac{p_{\text{III}}}{\rho_{\text{III}} R}$  is the constant temperature associated with the state of region III, with  $R = 287 \text{ J/kg-K}$  being the specific gas constant of the fluid, and  $T(r)$  is the temperature within the vortex:

$$T(r) = \begin{cases} A + \frac{\gamma - 1}{R\gamma} \frac{v_m^2}{a^2} \frac{r^2}{2}, & r \leq a, \\ B + \frac{\gamma - 1}{R\gamma} v_m^2 \frac{a^2}{(a^2 - b^2)^2} \left( \frac{r^2}{2} - 2b^2 \ln r - b^4 \frac{r^{-2}}{2} \right), & a < r < b, \\ T_{\text{III}}, & r \geq b, \end{cases}$$

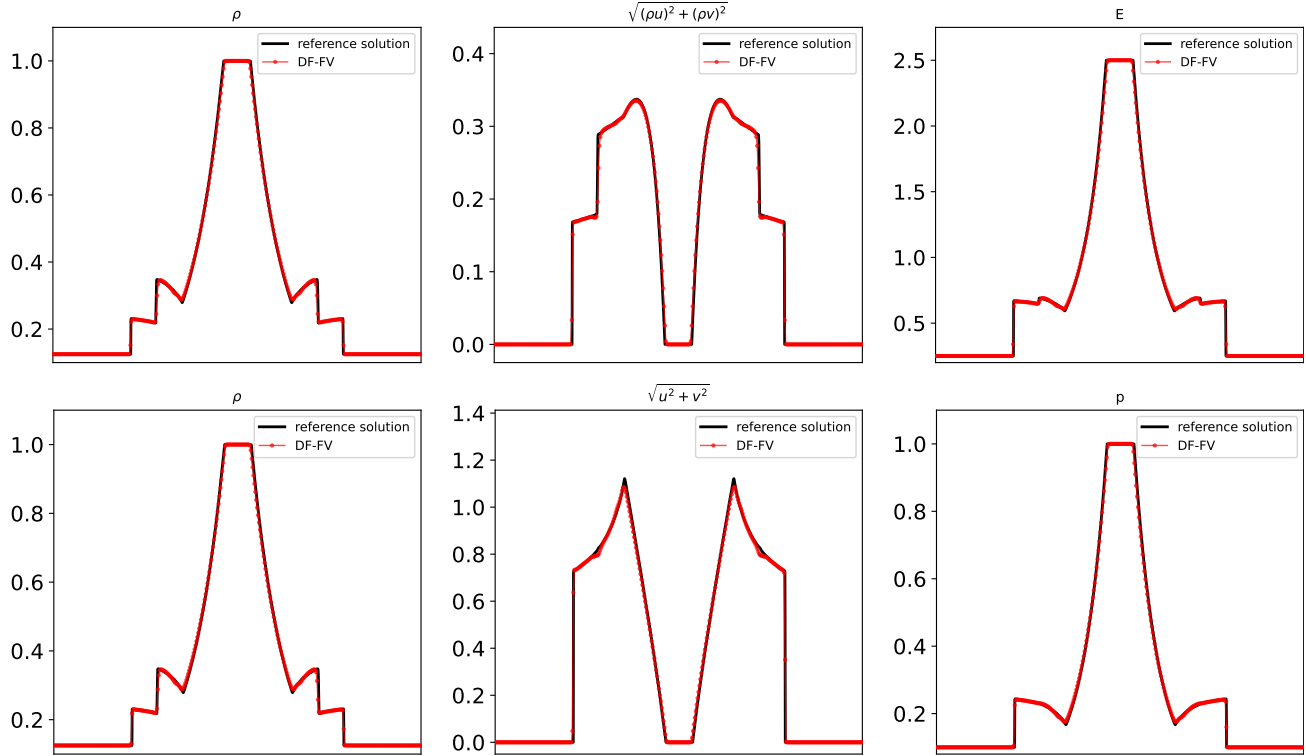


Figure 4.8: Example 6: 1-D slices along  $y = x$  for the  $\mathbf{U}$ -solution (upper row) and  $\mathbf{V}^x$ -solution (lower row).

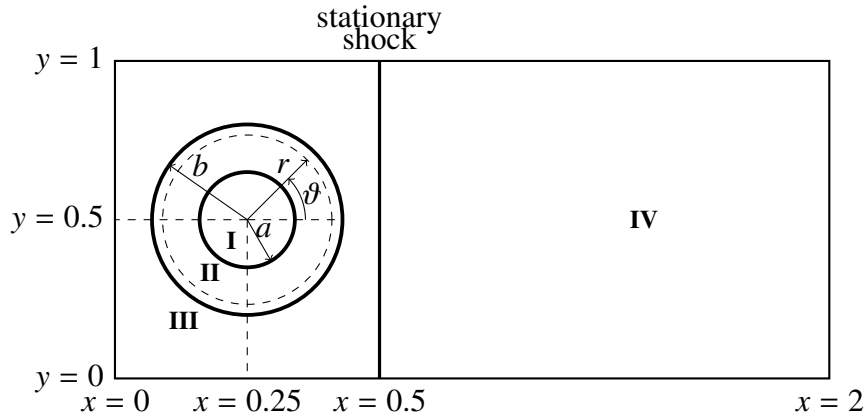


Figure 4.9: Example 7: Sketch of the simulation set-up.

where

$$B = T_{\text{III}} - \frac{\gamma - 1}{R\gamma} v_m^2 \frac{a^2}{(a^2 - b^2)^2} \left( \frac{b^2}{2} - 2b^2 \ln b - b^4 \frac{b^{-2}}{2} \right),$$

$$A = B + \frac{\gamma - 1}{R\gamma} v_m^2 \frac{a^2}{(a^2 - b^2)^2} \left( \frac{a^2}{2} - 2b^2 \ln a - b^4 \frac{a^{-2}}{2} \right) - \frac{\gamma - 1}{R\gamma} \frac{v_m^2}{2}.$$

Figure 4.10 shows a Schlieren image of the numerical results displaying the magnitude of the density gradient field,  $\|\nabla\rho\|_2$ , of the  $\mathbf{U}$ -solution computed on a uniform mesh with  $N_x = 1200$  and  $N_y = 601$  at time  $t = 0.7$  along with the reference solution obtained with the help of a seventh-order WENO-DeC

scheme from [36, 37], which was implemented using with reconstruction of characteristic variables and exact Riemann problem solver on a uniform  $800 \times 401$  mesh. In this figure, we have used the following shading function:

$$\exp\left(-\frac{K\|\nabla\rho\|_2}{\max\|\nabla\rho\|_2}\right), \quad K = 80,$$

where the numerical density derivatives are computed using central differencing.

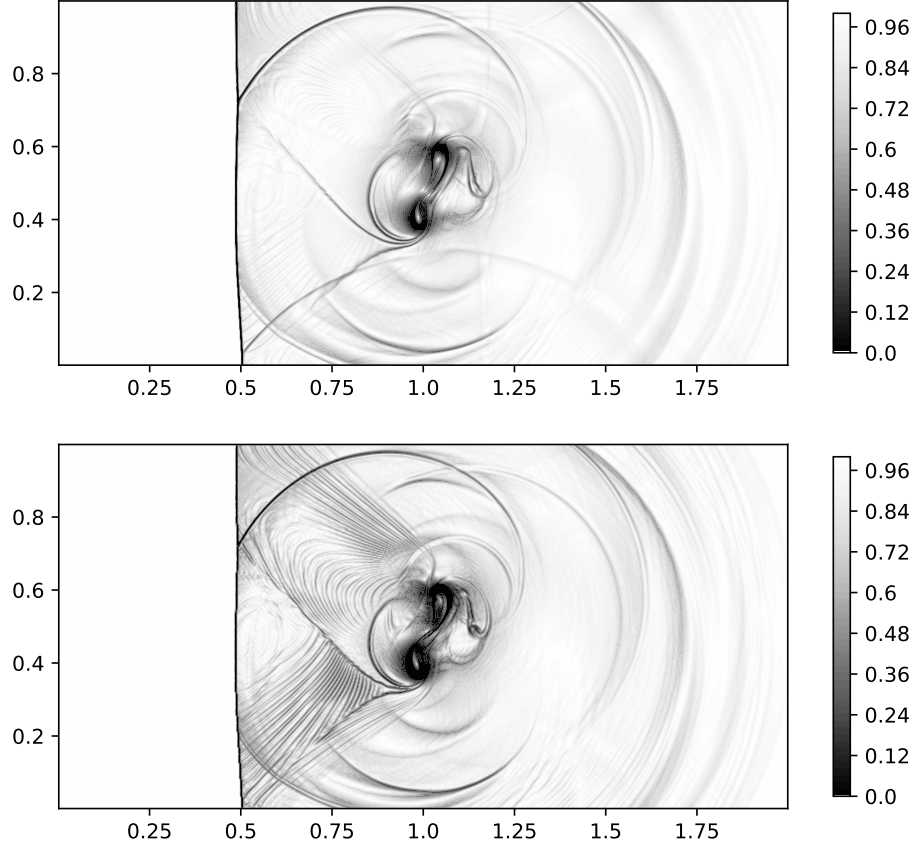


Figure 4.10: Example 7: Schlieren image of the density gradient of the DF-FV  $U$ -solution (top) along with the reference solution (bottom).

Clearly, the reference solution is more accurate and detailed than the DF-FV one. However, as one can see, all the relevant flow features are correctly captured by the DF-FV method. We note that the computed results also agree well with those obtained in the literature; see, e.g., [18].

**Example 8 (2-D Riemann problem).** In the last example, we consider the 2-D Riemann problem (Configuration 3) from [26] (also see [11]). In the computational domain  $[0, 1.2] \times [0, 1.2]$  with transmissive boundary conditions, we prescribe the following initial conditions:

$$V(x, y, 0) = \begin{cases} (1.5, 0, 0, 1.5)^T, & x > 1, y > 1, \\ (0.5323, 1.206, 0, 0.3)^T, & x < 1, y > 1, \\ (0.138, 1.206, 1.206, 0.029)^T, & x < 1, y < 1, \\ (0.5323, 0, 1.206, 0.3)^T, & x > 1, y < 1, \end{cases}$$

and we run the simulations on a uniform mesh with  $N_x = N_y = 1000$  until the final time  $t = 1$ . The obtained density component of the  $\mathbf{U}$ -solution is plotted in Figure 4.11. As one can see, the obtained result is consistent with that reported in [11], illustrating the ability of the DF-FV method to capture complex flow features of this benchmark.

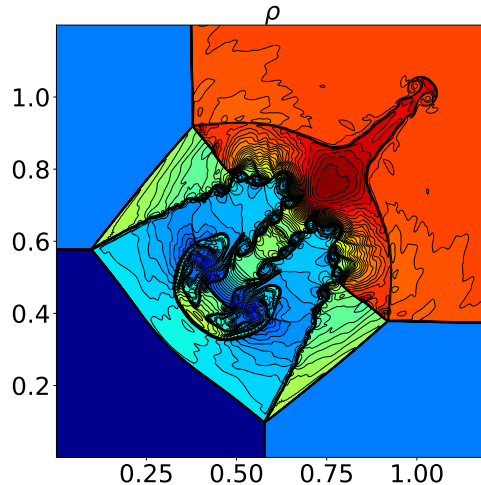


Figure 4.11: Example 8: Density-component of the  $\mathbf{U}$ -solution.

## 5 Conclusions

In this paper, we have introduced new methods for one- and two-dimensional hyperbolic systems of conservation laws, for which we consider two different formulations of the studied systems (the original conservative formulation and a primitive one containing nonconservative products), and discretize them on overlapping staggered meshes using two different numerical methods. Both the conservative and primitive variables are evolved in time using second-order semi-discrete finite-volume (FV) methods. The nonconservative system is discretized by a path-conservative central-upwind scheme, and its solution is used to evaluate very simple numerical fluxes for the original conservative system. The nonlinear stability of the resulting DF-FV methods is enforced with the help of a post-processing, which also guarantees a conservative coupling between the two sets of variables. The performance of the proposed methods has been demonstrated on a number of benchmarks.

The introduced DF-FV methods share an important feature with the AF formulation presented in [1]—the reliance on extra degrees of freedom used to discretize a nonconservative primitive formulation of the governing equations. On the other hand, several differences exist between the proposed approach and AF schemes.

- While DF-FV methods make use of cell averages of conserved and primitive variables on overlapping grids, AF schemes consider cell averages of the conserved variables and point values (either of conserved variables as in [16, 17] or primitive variables as in [1]) at cell interfaces.
- In the DF-FV methods, within each time evolution step, the primitive cell averages are evolved independently from the conserved ones, differently from the AF approach, in which the update of the point values makes an explicit use of the cell averages. This creates the need, within the DF-FV framework, for a suitable post-processing to reinstate the necessary coupling between the considered degrees of freedom.

On the other hand, such a decoupling may be beneficial. For example, having two sets of data for the discrete solution has been used to design a smoothness indicator based on the difference between these two solutions; see [10]. This smoothness indicator can be used to develop different adaptation strategies, which may substantially enhance the resolution achieved by the DF-FV method. In addition, we have been working on applications of the proposed framework to other problems, such as compressible multifluid flows, whose investigation is left for an upcoming paper.

- The 2-D DF-FV method relies on a different set of degrees of freedom from those used in the AF approach, as the 2-D DF-FV method does not consider degrees of freedom at cell nodes.

We would also like to emphasize that the main difficulty in designing higher-order extensions of the proposed DF-FV methods is related to developing a higher-order post-processing. Such post-processing should be based on a uniformly accurate reconstruction/interpolation. One can use, for example, CWENO reconstructions/interpolations (see [12, 13, 42] and references therein), and we plan to explore this possibility in our future work.

## Acknowledgment

R. Abgrall was partially supported by SNSF grant 200020\_204917 “Structure preserving and fast methods for hyperbolic systems of conservation laws”. The work of A. Chertock was supported in part by NSF grant DMS-2208438. The work of A. Kurganov was supported in part by NSFC grants 12171226 and W2431004. The work of L. Micalizzi was supported in part by the LeRoy B. Martin, Jr. Distinguished Professorship Foundation.

## In memoriam

This paper is dedicated to the memory of Prof. Arturo Hidalgo López (\*July 03<sup>rd</sup> 1966 - †August 26<sup>th</sup> 2024) of the Universidad Politécnica de Madrid, organizer of HONOM 2019 and active participant in many other editions of HONOM. Our thoughts and wishes go to his wife, Lourdes, and his sister, María Jesús, whom he left behind.

## References

- [1] R. ABGRALL, A combination of residual distribution and the active flux formulations or a new class of schemes that can combine several writings of the same hyperbolic problem: application to the 1D Euler equations, *Commun. Appl. Math. Comput.*, 5 (2023), pp. 370–402.
- [2] R. ABGRALL, Staggered schemes for compressible flow: a general construction, *SIAM J. Sci. Comput.*, 46 (2024), pp. A399–A428.
- [3] R. ABGRALL AND S. KARNI, A comment on the computation of non-conservative products, *J. Comput. Phys.*, 229 (2010), pp. 2759–2763.
- [4] R. ABGRALL AND Y. LIU, A new approach for designing well-balanced schemes for the shallow water equations: a combination of conservative and primitive formulations, *SIAM J. Sci. Comput.*, 46 (2024), pp. A3375–A3400.

- [5] W. BOSCHERI AND M. DUMBSER, Arbitrary-Lagrangian-Eulerian one-step WENO finite volume schemes on unstructured triangular meshes, *Commun. Comput. Phys.*, 14 (2013), pp. 1174–1206.
- [6] M. J. CASTRO, P. G. LEFLOCH, M. L. MUÑOZ-RUIZ, AND C. PARÉS, Why many theories of shock waves are necessary: convergence error in formally path-consistent schemes, *J. Comput. Phys.*, 227 (2008), pp. 8107–8129.
- [7] M. J. CASTRO, T. MORALES DE LUNA, AND C. PARÉS, Well-balanced schemes and path-conservative numerical methods, in *Handbook of numerical methods for hyperbolic problems*, vol. 18 of *Handb. Numer. Anal.*, Elsevier/North-Holland, Amsterdam, 2017, pp. 131–175.
- [8] M. J. CASTRO DÍAZ, A. KURGANOV, AND T. MORALES DE LUNA, Path-conservative central-upwind schemes for nonconservative hyperbolic systems, *ESAIM Math. Model. Numer. Anal.*, 53 (2019), pp. 959–985.
- [9] A. CHERTOCK, S. CHU, AND A. KURGANOV, Hybrid multifluid algorithms based on the path-conservative central-upwind scheme, *J. Sci. Comput.*, 89 (2021). Paper No. 48.
- [10] A. CHERTOCK, A. KURGANOV, AND L. MICALIZZI, New smoothness indicator within an active flux framework. Submitted; preprint is available at <https://chertock.wordpress.ncsu.edu/files/2025/05/CKM25.pdf>.
- [11] S. CHU, A. KURGANOV, AND I. MENSHOV, New adaptive low-dissipation central-upwind schemes, *Appl. Numer. Math.*, 209 (2025), pp. 155–170.
- [12] I. CRAVERO, G. PUPPO, M. SEMPLICE, AND G. VISCONTI, CWENO: uniformly accurate reconstructions for balance laws, *Math. Comp.*, 87 (2018), pp. 1689–1719.
- [13] I. CRAVERO, M. SEMPLICE, AND G. VISCONTI, Optimal definition of the nonlinear weights in multidimensional central WENOZ reconstructions, *SIAM J. Numer. Anal.*, 57 (2019), pp. 2328–2358.
- [14] G. DAL MASO, P. G. LEFLOCH, AND F. MURAT, Definition and weak stability of nonconservative products, *J. Math. Pures Appl. (9)*, 74 (1995), pp. 483–548.
- [15] M. DUMBSER, O. ZANOTTI, R. LOUBÈRE, AND S. DIOT, *A posteriori* subcell limiting of the discontinuous Galerkin finite element method for hyperbolic conservation laws, *J. Comput. Phys.*, 278 (2014), pp. 47–75.
- [16] T. EYMANN AND P. ROE, Active flux schemes for systems, 2011. In: 20th AIAA Computational Fluid Dynamics Conference, Paper No. 3840.
- [17] T. A. EYMANN AND P. L. ROE, Multidimensional active flux schemes, 2013. In: 21st AIAA Computational Fluid Dynamics Conference, Paper No. 2940.
- [18] M. GEISENHOFER, F. KUMMER, AND B. MÜLLER, A discontinuous Galerkin immersed boundary solver for compressible flows: adaptive local time stepping for artificial viscosity-based shock-capturing on cut cells, *Internat. J. Numer. Methods Fluids*, 91 (2019), pp. 448–472.
- [19] E. GODLEWSKI AND P.-A. RAVIART, Numerical approximation of hyperbolic systems of conservation laws, vol. 118 of *Applied Mathematical Sciences*, Springer-Verlag, New York, 2021. Second edition.

- [20] S. GOTTLIEB, D. KETCHESON, AND C.-W. SHU, Strong stability preserving Runge-Kutta and multistep time discretizations, World Scientific Publishing Co. Pte. Ltd., Hackensack, NJ, 2011.
- [21] S. GOTTLIEB, C.-W. SHU, AND E. TADMOR, Strong stability-preserving high-order time discretization methods, SIAM Rev., 43 (2001), pp. 89–112.
- [22] J. S. HESTHAVEN, Numerical methods for conservation laws, vol. 18 of Computational Science & Engineering, Society for Industrial and Applied Mathematics (SIAM), Philadelphia, PA, 2018. From analysis to algorithms.
- [23] T. Y. HOU AND P. G. LEFLOCH, Why nonconservative schemes converge to wrong solutions: error analysis, Math. Comp., 62 (1994), pp. 497–530.
- [24] A. KURGANOV AND C.-T. LIN, On the reduction of numerical dissipation in central-upwind schemes, Commun. Comput. Phys., 2 (2007), pp. 141–163.
- [25] A. KURGANOV, S. NOELLE, AND G. PETROVA, Semidiscrete central-upwind schemes for hyperbolic conservation laws and Hamilton-Jacobi equations, SIAM J. Sci. Comput., 23 (2001), pp. 707–740.
- [26] A. KURGANOV AND E. TADMOR, Solution of two-dimensional Riemann problems for gas dynamics without Riemann problem solvers, Numer. Methods Partial Differential Equations, 18 (2002), pp. 584–608.
- [27] P. G. LEFLOCH, Hyperbolic systems of conservation laws, Lectures in Mathematics ETH Zürich, Birkhäuser Verlag, Basel, 2002. The theory of classical and nonclassical shock waves.
- [28] P. G. LEFLOCH, Graph solutions of nonlinear hyperbolic systems, J. Hyperbolic Differ. Equ., 1 (2004), pp. 643–689.
- [29] R. J. LEVEQUE, Finite volume methods for hyperbolic problems, Cambridge Texts in Applied Mathematics, Cambridge University Press, Cambridge, 2002.
- [30] K.-A. LIE AND S. NOELLE, On the artificial compression method for second-order nonoscillatory central difference schemes for systems of conservation laws, SIAM J. Sci. Comput., 24 (2003), pp. 1157–1174.
- [31] Y. LIU, Central schemes on overlapping cells, J. Comput. Phys., 209 (2005), pp. 82–104.
- [32] Y. LIU, C.-W. SHU, E. TADMOR, AND M. ZHANG, Central discontinuous Galerkin methods on overlapping cells with a nonoscillatory hierarchical reconstruction, SIAM J. Numer. Anal., 45 (2007), pp. 2442–2467 (electronic).
- [33] Y. LIU, C.-W. SHU, E. TADMOR, AND M. ZHANG, Non-oscillatory hierarchical reconstruction for central and finite volume schemes, Commun. Comput. Phys., 2 (2007), pp. 933–963.
- [34] Y. LIU, C.-W. SHU, AND Z. XU, Hierarchical reconstruction with up to second degree remainder for solving nonlinear conservation laws, Nonlinearity, 22 (2009), pp. 2799–2812.
- [35] L. MICALIZZI, D. TORLO, AND W. BOSCHERI, Efficient iterative arbitrary high-order methods: an adaptive bridge between low and high order, Communications on Applied Mathematics and Computation, (2023), pp. 1–38.

- [36] L. MICALIZZI AND E. F. TORO, Impact of numerical fluxes on high order semidiscrete WENO-DeC finite volume schemes, *Sib. Electron. Math. Rep.*, 21 (2024), pp. B232–B287.
- [37] L. MICALIZZI AND E. F. TORO, Algorithms of very high space-time orders of accuracy for hyperbolic equations in the semidiscrete WENO-DeC framework, *J. Comput. Phys.*, 538 (2025). Paper No. 114167.
- [38] C. PARÉS, Numerical methods for nonconservative hyperbolic systems: a theoretical framework, *SIAM J. Numer. Anal.*, 44 (2006), pp. 300–321.
- [39] C. PARÉS, Path-conservative numerical methods for nonconservative hyperbolic systems, in *Numerical methods for balance laws*, vol. 24 of *Quad. Mat.*, Dept. Math., Seconda Univ. Napoli, Caserta, 2009, pp. 67–121.
- [40] R. M. PIDATELLA, G. PUPPO, G. RUSSO, AND P. SANTAGATI, Semi-conservative finite volume schemes for conservation laws, *SIAM J. Sci. Comput.*, 41 (2019), pp. B576–B600.
- [41] A. RAULT, G. CHIAVASSA, AND R. DONAT, Shock-vortex interactions at high Mach numbers, *J. Sci. Comput.*, 19 (2003), pp. 347–371. Special issue in honor of the sixtieth birthday of Stanley Osher.
- [42] M. SEMPLICE AND G. VISCONTI, Efficient implementation of adaptive order reconstructions, *J. Sci. Comput.*, 83 (2020), pp. Paper No. 6, 27 pp.
- [43] C.-W. SHU, Essentially non-oscillatory and weighted essentially non-oscillatory schemes for hyperbolic conservation laws, in *Advanced numerical approximation of nonlinear hyperbolic equations* (Cetraro, 1997), vol. 1697 of *Lecture Notes in Math.*, Springer, Berlin, 1998, pp. 325–432.
- [44] C.-W. SHU AND S. OSHER, Efficient implementation of essentially nonoscillatory shock-capturing schemes. II, *J. Comput. Phys.*, 83 (1989), pp. 32–78.
- [45] G. A. SOD, A survey of several finite difference methods for systems of nonlinear hyperbolic conservation laws, *J. Comput. Phys.*, 27 (1978), pp. 1–31.
- [46] P. K. SWEBY, High resolution schemes using flux limiters for hyperbolic conservation laws, *SIAM J. Numer. Anal.*, 21 (1984), pp. 995–1011.
- [47] E. F. TORO, *NUMERICA: A Library of Source Codes for Teaching, Research and Applications*, Numeritek Ltd., Cheshire, UK, [www.numeritek.com](http://www.numeritek.com), 1999.
- [48] E. F. TORO, *Riemann solvers and numerical methods for fluid dynamics: A practical introduction*, Springer-Verlag, Berlin, Heidelberg, third ed., 2009.
- [49] P. WOODWARD AND P. COLELLA, The numerical solution of two-dimensional fluid flow with strong shocks, *J. Comput. Phys.*, 54 (1984), pp. 115–173.
- [50] Z. XU, Y. LIU, H. DU, G. LIN, AND C.-W. SHU, Point-wise hierarchical reconstruction for discontinuous Galerkin and finite volume methods for solving conservation laws, *J. Comput. Phys.*, 230 (2011), pp. 6843–6865.
- [51] Z. XU, Y. LIU, AND C.-W. SHU, Hierarchical reconstruction for discontinuous Galerkin methods on unstructured grids with a WENO-type linear reconstruction and partial neighboring cells, *J. Comput. Phys.*, 228 (2009), pp. 2194–2212.